ACCSCIENCE PUBLISHING

Materials Science in Additive Manufacturing

REVIEW ARTICLE

Additive manufacturing of Inconel 939: A review of microstructure, defects, and mechanical properties

Pranjal Singh[1], Sheeza Khan[1], and A. Raja Annamalai[2]*

[1]School of Mechanical Engineering, Vellore Institute of Technology, Vellore, Tamil Nadu, India

[2]Centre for Innovative Manufacturing Research, Vellore Institute of Technology, Vellore, Tamil Nadu, India

***Corresponding author:**
A. Raja Annamalai
(raja.annamalai@vit.ac.in)

Citation: Singh P, Khan S, Annamalai AR. Additive manufacturing of Inconel 939: A review of microstructure, defects, and mechanical properties. *Mater Sci Add Manuf.* 2026;5(3):026080014. doi: 10.36922/MSAM026080014

Received: February 17, 2026

Revised: March 30, 2026

Accepted: April 3, 2026

Published online: June 19, 2026

Abstract

Additive manufacturing (AM) has created new possibilities to eliminate secondary processes such as machining. By reducing material waste and shortening lead times, AM is regarded as a key enabling technology for Industry 4.0 in the global market. Among nickel-based superalloys, Inconel 939 (IN939), a precipitation-hardened alloy, is widely explored for high-temperature components operating at service temperatures of ~850 °C in demanding aerospace applications such as gas turbine blades. The pronounced cracking susceptibility of IN939 introduces processing challenges in the AM environment. Fabricating dense components requires optimized processing parameters (laser power, scan speed, hatch spacing, and layer thickness). This review addresses the influence of AM routes—specifically powder bed fusion, directed energy deposition, and electron beam melting—on the microstructure and tensile properties of IN939. The mechanical performance of IN939 is primarily determined by the alloying element composition, with microstructural studies focusing on the formation of precipitate types. Mechanistic insights are provided that correlate the thermodynamic factors (solidification pathway and driving force for precipitation) and kinetic factors (cooling rate, diffusion) governing microstructural evolution with their influence on the strength-ductility trade-off. The compiled literature sheds light on the effects of heat treatment, the formation of various defect types, and fatigue and creep behavior of IN939.

Keywords: Additive manufacturing; Laser powder bed fusion; Inconel 939; Mechanistic modeling

1. Introduction

The scientific community is harnessing additive manufacturing (AM) to its fullest potential, as it simplifies the creation of complex geometries and enhances specific manufacturing processes and material properties.[1] AM technology can be traced to the invention of stereolithography by Chuck Hull in 1984 (foundational patent), followed by selective laser sintering[2,3] developed by Carl Deckard and patented in 1989. The concept of laser-based powder bed fusion (LPBF) was pursued by EOS in Germany (1989), introducing the first commercial laser sintering system (1990). By the late 1990s, powder bed fusion and directed energy deposition (DED) had emerged as two important AM processes.

The Inconel family was developed in the early 1930s by the International Nickel Company (INCO, founded in Canada) and is capable of sustaining high-temperature service in corrosive environments. Table 1 provides a chronological overview of the Inconel series. In 1930, Inconel 600, the first commercial alloy, exhibited solid-solution strengthening, non-magnetic properties, and resistance to oxidation across a wide temperature range from which subsequent alloys were derived.[4] In 1950, Inconel 713C was developed as a vacuum-melted precipitation hardened cast superalloy, in which the addition of Al and titanium (Ti) generates gamma prime (γ') precipitate.[5] In the early 1960s, two alloys were developed: Inconel 718, introduced in 1962, and Inconel 625, introduced in 1964. Inconel 718 is widely produced owing to its high tensile strength, which is regulated by the γ" precipitate (Ni_3Nb) and helps reduce the driving force for cracking during solidification.[6,7] Inconel 625 is solid-solution strengthened by molybdenum (Mo) and niobium (Nb) in the nickel (Ni)–chromium (Cr) matrix and exhibits high strength.[8]

Inconel 188 (Haynes 188), introduced in the mid-1960s, is a cobalt (Co)–Ni–Cr–tungsten (W) alloy designed for oxidation resistance at elevated temperatures, finding application in liners, ducts, and aero-engine gas turbines.[9] Inconel 690 was introduced towards the end of the 1960s and used in nuclear steam tubing, with a lower Co and higher Cr content. Inconel X-750, developed in the middle of the 20th century, became popular for its usage in turbine blades, seals, and high-temperature fasteners, due to its high oxidation and creep resistance.[10] Inconel 617, developed in the 1970s, is a solid-solution strengthened alloy by Co, Mo, and Cr; it offers high-temperature strength, oxidation and corrosion resistance with excellent weldability.[11] Alloys introduced during the 1980s extended the application range of the Inconel series. In 1982, Inconel 925 was invented, which improved mechanical properties and oxidation and corrosion resistance.[12] Thermally stable Inconel 230 was introduced in 1984 and was designed to be used in gas turbine combustors, heating systems, and chemical processes.[13] Inconel 725, designed to provide excellent corrosion protection, was introduced in 1989. Ti additions enable age hardening after heat treatment, thereby expanding the alloy's structural applications.[8] During the same period, Inconel 751, containing higher levels of aluminum (Al), enhanced the rupture strength of Ni alloys at high operating temperatures (~1,600 °F).[14] Inconel 939 (IN939) was developed in 1970,[15] with high Cr and Co content (18–20 wt%), providing superior oxidation and corrosion resistance for industrial gas-turbine applications. Previous studies have also supported the use of IN939 as a cladding material. The mechanical behavior is strongly governed by the volume fraction of the strengthening γ' precipitate. The alloying elements such as Al, Ti, tantalum (Ta), and Cr are essential for stabilizing γ' precipitates and ensuring long-term performance during high-temperature operations.

This review summarizes current insights on IN939 developed via different powder-bed fusion techniques, focusing on the microstructure-strength relationship. LPBF, which is of great interest to automotive and aerospace applications[16], is considered an ideal processing route for the fabrication of components.[17–19] The optimal processing route is application-driven, with the cooling rate factor playing a vital role. High cooling rate, on the order of 10^5–10^6 K/s, controls microstructural stability. Furthermore, LPBF enables the fabrication of conformal cooling channels with high geometric resolution, allowing more uniform heat extraction. The fine-powder bed resolution enables the production of intricate geometries with a fully enclosed interior cavity without support structures. DED, by comparison, lacks resolution, and electron beam melting is constrained by a larger powder size.

1.1. Laser powder bed fusion

The LPBF method is used to print three-dimensional parts by continuously adding thin layers of material, guided by a digital approach. This process involves designing complex geometry using computer-aided design (CAD) and an automated batch system. Computer-aided manufacturing and controlled material deposition are used to achieve the accuracy of the built part. LPBF is an AM process that builds parts with complex geometries layer by layer from CAD-designed models.[1,2] Figure 1 shows how LPBF works by using a laser to melt metal powder within the powder bed selectively. During this process, a thin layer of metal powder is evenly spread across the build platform, and a focused laser melts it. Support structures are formed from the unmelted powder remaining in the bed.[20] The build platform moves downward as each layer solidifies, allowing another layer to be deposited on top of the solidified surface.[21] This process features rapid solidification rates of approximately 10^5–10^7 K/s[3]. When LPBF is combined with heat treatment, it improves the application of IN939 in the aerospace industry. To fully utilize the properties of LPBF-produced IN939, standard heat treatment involving solutionizing is performed. This process dissolves γ' phases formed during LPBF, resulting in a supersaturated solid solution, and removes η phases.[22,23] To further enhance properties, aging is conducted, which promotes γ' phase growth, the primary strengthening mechanism of IN939.[22,24]

Table 1. A chronological overview of Inconel alloy: Strengthening mechanism and application

Alloy	Year	Strengthening mechanism	Application
IN600	1930	Solid solution (Ni–Cr–Fe)	Oxidation/corrosion-resistant heat exchangers and process equipment
IN713C	1950s	Precipitation (γ', Ni_3(Al, Ti))	Vacuum-cast turbine blades and vanes
IN718	1962	Precipitation (γ", Ni_3Nb)	Aerospace turbine discs, shafts, casings, and fasteners
IN625	1964	Solid solution (Mo, Nb in Ni–Cr)	Marine, chemical processing, and aerospace structural components
IN188	1966	Solid solution (Co–Ni–Cr–W)	Combustion liners, transition ducts, and afterburner hardware
IN690	~1968	Solid solution (high Cr, ~30 wt%)	Nuclear steam generator tubing; chemical plant heat exchangers
IN X-750	Mid-20th century	Precipitation (γ', Ni_3 (Al, Ti))	Turbine blades, seals, springs, and high-temperature fasteners
IN617	1970	Solid solution + carbide (Co, Mo, Cr)	Reformer tubes, combustors, and high-temperature heat exchangers
IN939	1970	Precipitation (γ', Ni_3 (Al, Ti, Ta))	Industrial gas turbine vanes and blades; weld-repairable hot-section components
IN925	1982	Precipitation (γ'/γ", Ti and Al addition)	Oil and gas wellbore completion components
IN230	1984	Solid solution + carbide (W, Mo)	Combustors, industrial heating systems, and high-temperature reactors
IN725	1989	Precipitation (γ'/γ", Ti and Nb addition)	Sour-gas wellbore components in high-pressure/high-temperature service
IN751	~1989	Precipitation (γ', Al-rich Ni_3Al)	Exhaust valves; high-temperature rupture-strength applications

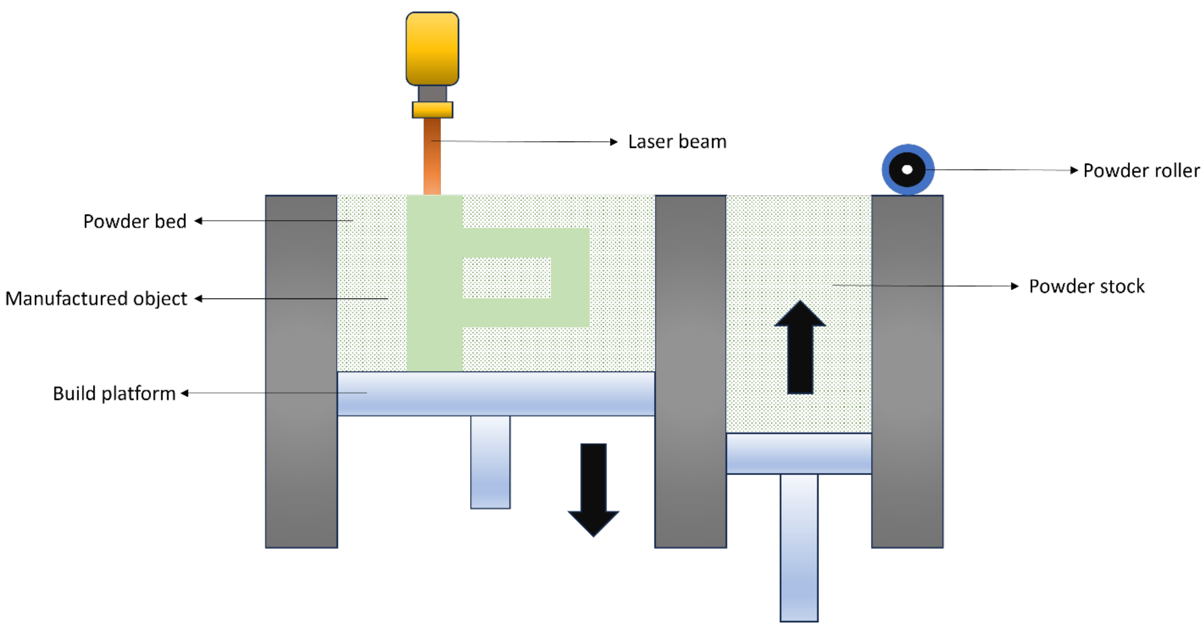

Figure 1. Process overview of laser powder bed fusion

1.2. Directed energy deposition

Directed energy deposition is an AM process. Figure 2 illustrates the working principle, which uses a focused heat source produced by a laser or electron beam to melt the deposited material.[25,26] DED printers have a nozzle head that can move in multiple directions around an object, based on a CAD model, depositing material along the required areas. The focused energy source melts the delivered feedstock and a portion of the substrate, forming a melt pool that solidifies into a deposited track. A continuous layer-by-layer process is followed until the object is complete. The solidification rate for this process ranges from 10^3 to 10^5 K/s.[27–29] This process is used for large-scale printing and has a high deposition rate, making it a cost-efficient technique.[30]

1.3. Electron beam melting

Electron beam melting is a three-dimensional (3D) printing method in which metal powder is held in a vacuum chamber and melted by an electron beam.[30] Figure 3 shows that this process requires a high-energy electron beam and a vacuum chamber to prevent oxidation, which can cause deterioration of the finished parts.[20,31,32] The powder on the bed is first preheated, sintered, and then melted. The bed is lowered so a new layer of powder can be laid on top, and this process repeats until the final part is created.[33] This process operates at high temperatures, around 1,000 °C, affecting phase formation through solidification and solid-state transformations.[34] Electron beam melting has a cooling rate of up to 10^2–10^3 K/s.[35] The grain size can vary with location, current, electron-beam velocity, and cooling rate. This variation promotes heterogeneous nucleation and grain-size refinement before solidification.[36] The process provides low thermal gradients and residual stresses.[37] Metal powder is processed as a feedstock by DED, LPBF, binder jetting, selective laser melting (SLM), and electron beam melting.

1.4. Effects of alloying elements

Nickel-based superalloys are composed of 8–10 elements, each with a specific role. Here, we focus on IN939, which is traditionally known as a Ni–Cr alloy, as Cr is its most significant element. Ni, present in the highest percentage, forms the γ matrix. After Cr, Co is the next most abundant element, which leads to the formation of various secondary phases, precipitates, and deleterious phases at different temperatures.[38–44] In IN939, the γ phase begins to form early at approximately 63 wt% at 600 °C. The γ matrix has a face-centered cubic (FCC) crystal structure with the space group Fm-3m (No. 225).[45,46] Ti, Ta, and Al promote the formation of γ' precipitate, i.e., (Ni_3(Al, Ti)).[47–49] The γ' phase forms up to ~35 wt% at 600 °C[24] and serves as a high-temperature strengthening phase in superalloys.[48] It possesses FCC $L1_2$ crystal structure (space group Pm-3m [No. 221]), where Al/Ti atoms occupy corner positions while Ni atoms reside at face-centered positions.[44,45,50,51] γ" precipitates, which have a body-centered tetragonal structure with the space group I4/mmm (No. 139), formed through Nb addition and commonly expressed as Ni_3Nb. Strengthening performance occurs due to the γ' and γ" barriers limiting dislocation movement, which requires additional energy.[49,52–54] Table 2 shows the phases, crystal structure, and space group for the respective precipitates

Table 2. Phases, crystal structure, and space group of Inconel 939

Phase	Crystal structure	Composition	Space group
γ matrix	FCC	Ni, Co, Nb, Cr, Fe	Fm-3m (No. 225)
γ'	$L1_2$ ordered FCC	Ni_3(Al, Ti)	Pm-3m (No. 221)
γ"	BCT	Ni_3Nb	I4/mmm (No. 139)
MC, $M_{23}C_6$	FCC	MX (Nb, Ti, etc.) and $M_{23}C_6$ types	Fm-3m (No. 225)
η	HCP, $D0_4$ structure	Ni_3Ti or Ni_3Ta	$P6_3$/mmc (No. 194)
σ	Tetragonal	(Ni, Co, Cr, Mo, W, Ta, Nb)	$P4_2$/mnm (No. 136)
Laves	Hexagonal (C14)	$(Ni, Fe, Cr)_2$ (Nb, Mo, Ti)	$P6_3$/mmc (No. 194)

Abbreviations: BCT: Body-centered tetragonal; FCC: Face-centered cubic.

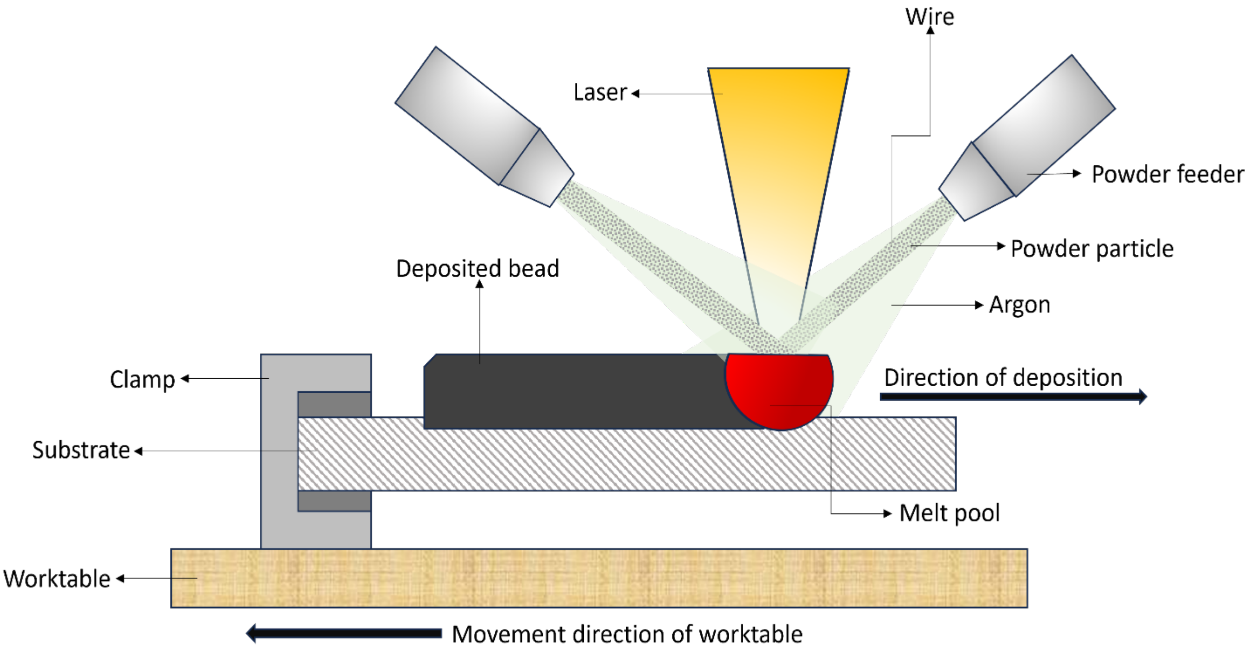

Figure 2. Overview of directed energy deposition

present in IN939. A small amount of carbon is added, forming MC-type carbides or $M_{23}C_6$ carbides, which have an FCC crystal structure and the Fm-3m (No. 225) space group.[53,55] The precipitates are solidification-stable at a concentration of about 1–2 wt% and will remain unchanged over a wide temperature range, which is useful for creep resistance, allowing stress relaxation and limiting grain boundary sliding at high temperatures.[23,53,55] They dissolve at temperatures around 1,320 °C.[23] Some deleterious precipitates, such as η (Ni_3Ti with Ta, Nb, Al), are also formed, which deteriorate the material by causing embrittlement, reducing ductility, and affecting creep life. This η phase has a hexagonal D024 crystal structure with space group $P6_3/mmc$ (No. 194). It forms around 911 °C, with its wt% increasing up to ~5% at 1,050 °C, before dissolving completely at around 1,134 °C.[23] Other precipitates, such as Laves and sigma phases, also exist, with topologically close-packed hexagonal and tetragonal crystal structures, assigned space groups $P6_3/mmc$ (No. 194) and $P4_2/mnm$ (No. 136), respectively.[47,49,52] Each element in IN939 is crucial in enhancing the overall material performance.

2. Overview of the structural integrity of laser powder bed-fused IN939

The mechanical behavior of IN939, widely used in the aviation sector for making turbine blades and vanes, is heavily influenced by thin-walled geometries, especially during LPBF manufacturing. Experimental research and application-based studies on conventionally processed IN939 have shown that the component's thickness plays a crucial role in tensile strength, with a consistent decrease in tensile strength as thickness decreases. This dependence has also been observed in variants of additively manufactured materials, with the critical importance of wall thickness to the mechanical performance of LPBF-produced IN939 parts.[15,56] Research has also focused on the effects of temperature changes on the mechanical properties of superalloys, as illustrated in Table 3. It shows that elongation and tensile strength decrease with increasing temperature. This decrease is primarily due to increased dislocation motion, as more thermal energy is required to activate slip systems.[57] In addition, studies on silicon (Si) alloying have examined the crack reduction behavior of IN939. Although earlier studies reported reduced crack density at lower Si content, more recent work suggests that controlled Si addition within a specific composition range can reduce cracking by altering crystallographic orientation and grain refinement. The microstructural modification, the primary dendritic arm spacing increases with the addition of Si, leading to a drop in cooling rate during LPBF.[25] The associated increase in solidification time reduces thermal stresses, thereby lowering the susceptibility to solidification cracking. Experimental research shows that AM has higher tensile strength at three temperatures compared to traditional casting. In

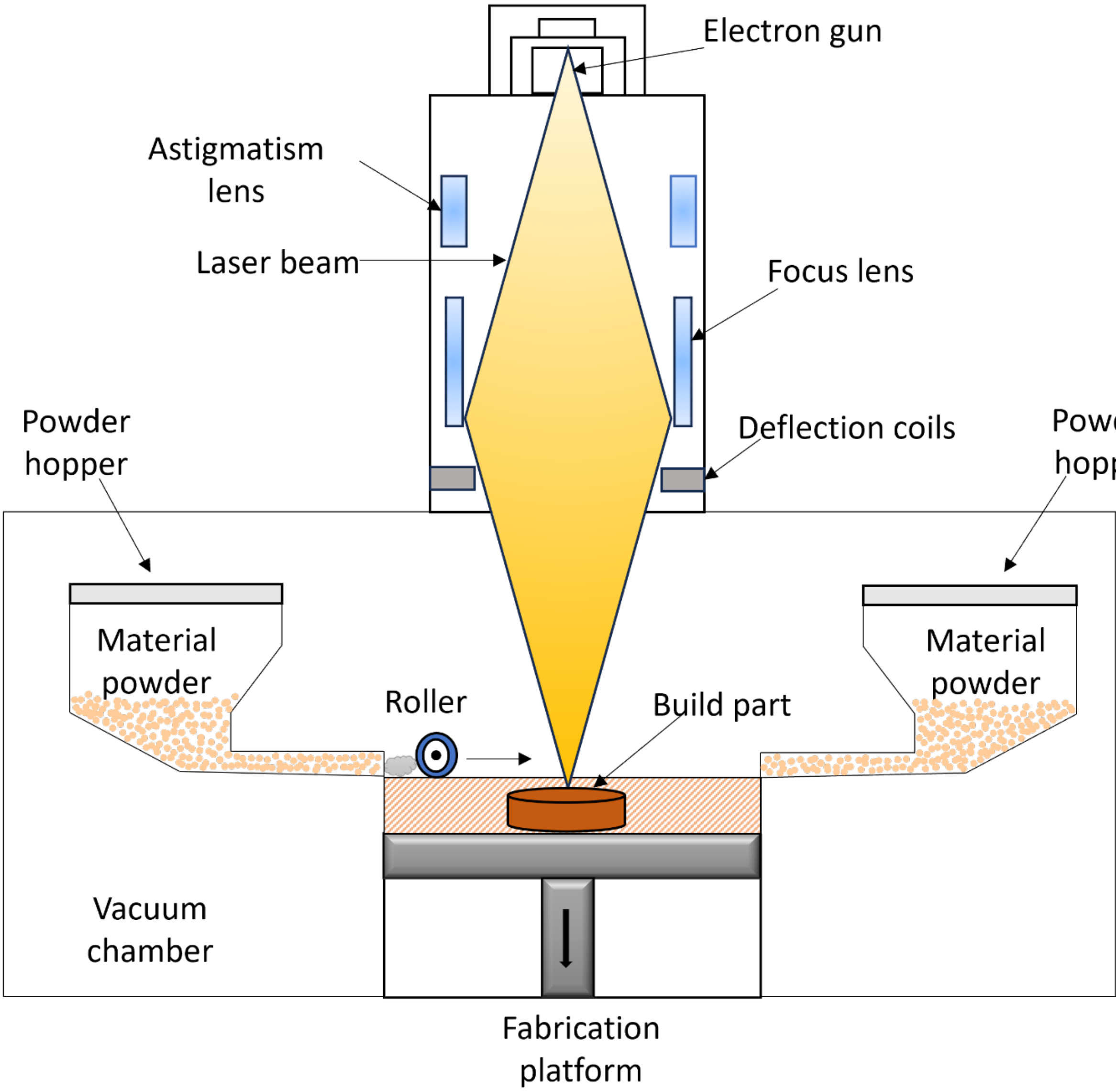

Figure 3. Process overview of electron beam melting

addition, tensile strength is also significantly enhanced by the formation of spherical γ' precipitates in samples produced by AM subjected to heat treatment.[58] Tensile tests at three different temperatures revealed that secondary γ' precipitates are primary contributors to increased strength, as they act as obstacles to dislocation motion and, as a result, restrict the slip and enhance the alloy strength.[59] The differences in the macro and microstructures of IN939 significantly influence its tensile performance. It is important to preheat at about 400 °C, which increases the solidification time and allows more time to carry out crystallization and promotes the formation of carbides and γ' precipitates, thereby improving alloy strength. These precipitates directly affect the mechanical properties, either enhancing or degrading performance depending on their size and volume fraction.[60–64] The properties of IN939 have been investigated using techniques such as wire electric discharge machining (W-EDM). Different build orientations of the alloy have shown anisotropic behavior under various W-EDM parameters, e.g., pulse-on and pulse-off periods. It is interesting to note that the Z-direction exhibits lower tensile strength than the XY-plane, which is attributed to differences in grain growth and microstructural evolution. Microstructural changes in the Z-direction, due to the formation of elongated grains, directly influence mechanical performance.[65–69] Solution treatments have also been studied to understand their effects on the mechanical properties of LPBF-manufactured IN939. The findings indicate that tensile properties are not always improved by solution treatment alone. The formation of larger recrystallized grains with intragranular carbides can create preferential sites for crack initiation and reduce mechanical performance. Consequently, the Heat Treatment 2 (HT2) condition does not exhibit improved room-temperature strength. Additionally, comparisons between Heat Treatment 1 (HT1) and HT2 samples reveal that tensile strength decreased under both conditions. These findings suggest that solution treatment alone is insufficient; further aging is necessary to promote γ' precipitation and enhance IN939's strength.[63,70,71]

The mechanical behavior and microstructural development of LPBF-processed IN939 under various heat treatment pathways, such as direct aging and solutioning followed by aging, have been studied in recent research. Unlike in the solutionized and two-step-aged conditions, the γ' precipitate size varied significantly between the solutionized and water-quenched states. Tensile strength improved at room temperature under direct aging conditions (DA1 and DA2), although ductility decreased. The water-quenched samples provided a better combination of mechanical properties, showing a more favorable balance between high strength and moderate ductility.[57,72–74]

Table 3. The reported tensile strength of additively manufactured Inconel 939

No.	Author	Condition/parameter	Tensile strength (MPa)	References
1.	Fardan *et al.*	0.5 mm thickness; 90° orientation	932	56
		0.5 mm thickness; 45° orientation	955	
		1 mm thickness; 90° orientation	1,269	
		1 mm thickness; 45° orientation	1,134	
		2 mm thickness; 90° orientation	1,331	
		2 mm thickness; 45° orientation	1,204	
2.	Zou *et al.*	Room temperature (RT)	1,437	57
		650 °C	960	
		700 °C	880	
		850 °C	400	
		950 °C	200	
3.	Zhang *et al.*	IN939	1,000	25
		IN939 + 1.5% Si	1,100	
		IN939 + 3% Si	1,200	
4.	Shaikh *et al.*	Direct aged	1,429	75
		Solution+aged	1,438	
5.	Šulák *et al.*	23 °C	1,106	58
		700 °C	936	
		800 °C	786	

(*Cont'd...*)

Table 3. (*Continued*)

No.	Author	Condition/parameter	Tensile strength (MPa)	References
6.	Gusain *et al.*	HT1	1,450	59
7.	Malý *et al.*	Room temperature	1,074	60
		400 °C	1,341	
		200 °C	1,062	
8.	Li *et al.*	Hot isostatic pressing	1,153	62
9.	Kanagarajah *et al.*	Aged	1,286	64
10.	Piwowarski *et al.*	HT1	1,410	71
11.	Kumar *et al.*	DA2	1,236	73

3. Microstructural relationship of Inconel 939

The Gibbs energy characteristics of the Ni–Cr binary system help explain the stability of the FCC phase of IN939. Precipitation hardening is the primary method used to strengthen IN939, which has an FCC austenitic matrix as its continuous phase. Its mechanical performance is improved by appropriate proportions of alloying elements such as Co, Cr, Mo, and W incorporated into this matrix.[16]

Table 4. Selected studies on the microstructure of Inconel 939

No.	Author	Microstructure description	Optical microscopy image	References
1.	Visibile *et al.*	Melt pool morphology with 100–200 μm width, along with laser tracks corresponding to the build direction	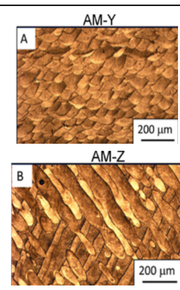	76
2.	Piwowarski *et al.*	After HT1, elongated grains were observed in the sample, and a melt pool was also seen, which shows uniform dendritic morphology	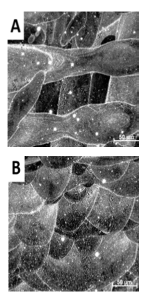	71

(*Cont'd...*)

Table 4. (*Continued*)

No.	Author	Microstructure description	Optical microscopy image	References
3.	Marchese *et al.*	Melt-pool boundaries defining fish scale structure with dominant columnar grains	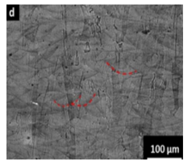	24
4.	Malý *et al.*	Uniform melt pools and laser tracks are seen in the XZ and XY axes, respectively, with columnar grains elongated along the build direction	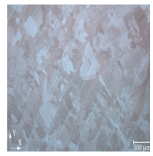 	60
5.	Rodríguez-Barber *et al.*	Fine cellular structure defining columnar grains with <001> texture	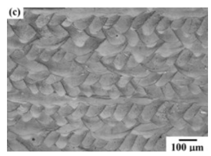	77
6.	Fardan *et al.*	Half-circle melt pool borders are observed in the microstructure that are non-uniform, which is formed due to a 67° scan rotation that produces partly melted particles, resulting in surface roughness	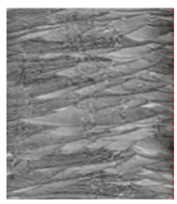	56

The FCC crystal structure has the highest atomic packing efficiency, ~74%, providing multiple slip systems.[78] Gibbs free energy (G), defined as:

$$\Delta G = \Delta H - T\Delta S \tag{1}$$

where ΔH is the enthalpy change, T is the absolute temperature, and ΔS is the entropy change. This relationship helps explain the thermodynamic stability of the FCC phase. Gibbs free energy represents the amount of a system's internal energy available to perform work at constant temperature and pressure. Since FCC can accommodate a wide variety of substitutional solutes, the increase in configurational entropy in the IN939 FCC matrix complements the enthalpic decrease due to dense atomic packing. The thermodynamic stability of the FCC phase in Ni-based superalloy IN939 is maintained by the reduction of Gibbs free energy through the combined effects of lower enthalpy and higher entropy.[79] Ni and Cr are the primary alloying elements in IN939, forming the basis for its phase stability. While Cr is stable in the body-centered cubic crystal structure, Ni exhibits a stable FCC crystal structure. The Ni–Cr binary phase diagram shows that at about 1,200 °C, Ni and Cr (Ni(Cr)) form a substitutional solid solution that maintains the FCC structure. Conversely, Cr (Ni), which stabilizes in the body-centered cubic structure, forms when Cr dissolves Ni. The alloy system is expected to be thermodynamically stable at high temperatures because both solid solutions correspond to regions of reduced Gibbs free energy. This stability is facilitated by the extensive FCC solid–solution zone in the Ni–Cr system, which forms the matrix phase in Ni-based superalloys such as IN939.[80]

Inconel 939 is a high-performance superalloy that offers high strength at high temperatures. It has several phases in its microstructure, including carbides, solid–solution constituents, and strengthening precipitates, which are the major contributors to its strength. To stabilize these phases and improve mechanical performance, alloying elements such as W, Ta, and Nb are also added.[80,81] These strengthening mechanisms are promoted in the FCC crystal structure using the γ-phase matrix. Several processing and heat-treatment methods have been studied to further enhance its properties, which require detailed microstructural analysis. Table 4 illustrates the existing literature on the microstructural morphology of IN939. Kanagarajah *et al.*[64] analyzed microstructures along and across the build direction of IN939 samples made via LPBF. The study found that layer-by-layer AM forms homogeneous, archlike structures along the melt-pool boundaries.[64] As-built IN939 samples exhibit a wide range of microstructural variability at different volumetric energy densities (VEDs). Rodríguez-Barber *et al.*[77] found that high VED favors the development of columnar grains characterized by a unique and uniform texture compared to weakly textured polycrystals with randomly shaped grains produced at low VED.[77] The sensitivity of additively manufactured IN939 to processing parameters reflects the significant role of energy input in tailoring the microstructure.[80]

In LPBF-processed IN939, Güler *et al.*[82] reported that arch-shaped melt pools with dendritic and interdendritic structures, which contribute to anisotropic mechanical behavior, can be observed.[82] Additional observations by Zhang *et al.*[25] were that pure IN939 often cracks along the build direction, whereas carefully controlled Si additions greatly suppress cracks, and even crack-free alloys can be obtained. Si acts as a surface-active element and can alter melt-pool dynamics at concentrations of 1.5–3.0 wt%. Its incorporation inhibits the solidification cracking mechanism. It was noted that a shift in microstructural evolution occurred, with the main cracks in columnar grains becoming the dominant feature. As the Si content increases, the optical micrographs show negligible cracking. This behavior is attributed to Si segregation, which modifies the surface tension coefficient and alters the Marangoni convection. Additionally, the overall mechanical response of the alloy improved with a faster cooling rate and increased precipitation, which was richer in Ti, Si, and Nb[25]. Piwowarski *et al.*[71] studied the as-built microstructure of IN939 and found that it formed dendrites within melt pools that were rotated by 67° between successive layers. Heat-treated conditions (HT1 and HT2) have been examined; these show equiaxed grains in the XY plane and elongated grains in the XZ plane. Dendritic features disappeared after heat treatment, and HT2 exhibited fully recrystallized grains of the same size in both planes. The as-printed condition had similar melt pools, with depths of approximately 40 to 50 μm in longitudinal and transverse directions, as reported by Kumar *et al.*[83] Columnar grains averaging approximately 104 μm in length were observed in the longitudinal slice after heat treatment, highlighting the significant effect of heat treatment on grain shape. Malý *et al.*[60] discovered diverse microstructural properties of IN939 depending on the observation plane. Regular melt pools were observed in the XZ plane, while laser scan trails appeared in the XY plane. The substrate was preheated to 400 °C, producing fine cellular structures and columnar grains extending along the build direction; in some areas, the columnar grains developed perpendicular to the build. Marchese *et al.*[24] identified lengthy grains aligned with the build direction, with dendritic, interdendritic, and submicrometric phases grouped near grain borders. These results suggest that while rapid solidification inhibits the formation of these features, they appear under more gradual cooling conditions. The microstructure of cylindrical IN939 samples was optimized by Kumar *et al.*[72], who found that the as-printed state exhibited dendritic-columnar characteristics with Ti- and Nb-rich phases and metal carbides along grain boundaries. In DA1, additional double-aging treatments (DA1 and DA2) promoted the precipitation of γ' and carbides, whereas in DA2, η (Ni_3Ti) and γ' phases formed. At a 67° scan rotation, Fardan *et al.*[56] observed semi-circular, irregular melt pools, with partly melted powder particles contributing to surface roughness. Shaikh *et al.*[75] found dendritic and fine interdendritic structures alongside elongated columnar grains oriented along the build direction in parallel sections. In their comparison of AM- and traditionally fabricated IN939, Visibile *et al.*[76] attributed the microstructure differences to variations in heat flow, which lead to anisotropic characteristics. While AM-Z (perpendicular to the build direction) exhibited clear elongated grains, indicating orientation-dependent microstructural development in AM alloys, AM-Y (parallel to the build direction) contained melt pools 100–200 μm in size without affecting the orientation of columnar grains.

4. Effect of heat treatment on IN939

The heat treatment approaches adopted modify the solidification behavior, thermal gradient, and undercooling, significantly affecting the ultimate tensile strength (UTS), grain morphology, size, and distribution of γ' precipitates. These heat-treatment regimes are primarily designed to strengthen by controlling γ' precipitation and dissolving deleterious phases. Therefore, the initial treatment involves single-phase formation, so that the deleterious and unwanted precipitates are dissolved, a process known as solutionizing. Subsequent aging steps employed primarily for IN939 include single-step, two-step, or four-step direct aging from the as-printed condition. Solutionizing of IN939 is usually carried out at two temperature variants (1,160/1,190 °C, 4 h). To reduce the porosity, a direct heat treatment method can also be adopted, which operates within the range of 1,163–1,200 °C/3 h. The cooling environment also plays a vital role, and common cooling methods include water quenching (WQ), air cooling (AC), and furnace cooling (FC), each of which affects microstructural evolution differently. WQ effectively freezes the microstructure. During solutionizing, various processing routes can be adopted; however, for precipitate evolution, rapid AC is generally adopted. Table 5 consolidates the overview of different heat treatment regimes. Shaikh *et al.*[23] investigated the microstructural behavior with and without solutionizing. In the as-printed condition, γ' precipitates were absent, whereas a dendritic microstructure was observed along the build direction. Direct aging, i.e., without solutionizing, leads to the formation of the η phase, which affects ductility. Microstructure and tensile performance are systematically influenced by processing strategy and post-build heat treatment, according to published research on additively manufactured IN939. LPBF IN939 microstructural behavior in the as-printed condition was investigated by Shaikh *et al.*[75], and the necessity for solutionizing was also assessed. Aging without solution treatment (1,000 °C/6 h + 700 °C/16 h) resulted in columnar cellular grains with γ' sizes of 200–300 nm and a UTS of 1,429 ± 35 MPa (low ductility ~4.6% attributed to induced embrittlement), while solution treatment at 1,190 °C/4 h before aging led to a strength of 1,438 ± 10 MPa. According to Šulák *et al.*[58], the LPBF built in both horizontal and vertical orientation and heat-treated at 1,160 °C/4 h, then 1,000 °C/6 h + 800 °C/4 h, exhibited strong anisotropic texture and columnar <001> grains with UTS values of about 1,050–1,150 MPa, yield strengths of about 850–950 MPa. Gusain *et al.*[59] reviewed studies, the highest equiaxed grains were obtained through the combination of LPBF with hot isostatic pressing (HIP) and a multi-step HT3, which comprised stress relief at 900 °C, solution treatment at 1,190 °C, followed by aging. This yielded a bimodal γ' distribution, with primary γ' ~205 nm and secondary γ' ~20 nm; corresponding to this, the UTS was ~1,200 MPa, and the yield strength was 900 MPa. Although γ' size was not specifically stated, Malý *et al.*[60] demonstrated that LPBF with base-plate preheating at 400 °C produced larger melt pools and wider columnar grains in the as-built condition, yielding a UTS of ~1,250 MPa. Kumar *et al.*[72] studied that in LPBF IN939, direct aging at 800 °C/6 h produced fine γ' precipitates of 25–30 nm and a yield strength of 1,040 ± 6 MPa while maintaining the cellular–columnar structure. Higher-temperature direct aging at 1,000 °C/6 h followed by aging promoted η-phase formation with γ' coarsening to ~250 nm and increased yield strength to 1,235 ± 26 MPa without changing grain morphology. While AC produced ~50 nm γ' and minor sub-cell coarsening, solution treatment at 1,190 °C/4 h followed by FC promoted γ' coarsening to ~100–200 nm without recrystallization. While furnace-cooled conditions produced coarser γ' of ~250–300 nm, intricate routes combining WQ and double aging produced optimized γ' distributions of ~80–100 nm with yield strengths around 930 MPa, consistently retaining the cellular columnar grain morphology. According to Kumar *et al.*[83], LPBF IN939 exhibited high tensile strengths of 1,403 ± 11 MPa in the transverse direction and 1,385 ± 4 MPa longitudinally, with γ' sizes in the range of 80–180 nm, after undergoing solution treatment at 1,190 °C/4 h and aging at 1,000 °C/6 h + 800 °C/4 h. On the other hand, Kanagarajah *et al.*[64] found that SLM-fabricated IN939 underwent significant recrystallization after being treated at 1,160 °C for 4 h and then aged at 850 °C for 16 h. This resulted in equiaxed grains of about 35–70 μm with a weakened texture and UTS values between 1,150 and 1,250 MPa. In SLM-fabricated IN939, Güler *et al.*[82] compared HIP-assisted aging (HT1) and vacuum heat treatment aging (HT2), reporting γ' volume fractions of ~31.6% and ~32.1%, respectively, with corresponding UTS values of ~760–780 MPa and ~750–770 MPa; HT1 caused directional coarsening and platelet-like distortion, while HT2 encouraged spherical coalescence and partial dissolution of γ'. Li *et al.*[62] showed that electron beam selective melting-fabricated IN939 subjected to HIP at 1,200 °C + 4 h + 120 MPa (FC) achieved a UTS of 1,153 ± 50 MPa with homogenized columnar grains, whereas HIP + HT at 1,140 °C/4 h followed by aging at 850 °C/16 h produced homogeneous γ' precipitates below 200 nm and a reduced UTS of 987 ± 116 MPa. HT1 (1,120 °C/4 h + 1,000 °C/6 h + 800 °C/4 h) produced a plate-like η phase and coarsened primary γ' of ~2 μm, whereas HT2 (1,120 °C/4 h + 850 °C/8 h + 750 °C/8 h) produced spherical primary γ' with sizes of ~70–120 nm and a γ' volume fraction of ~30.6%, according to Ozer *et al.*[84] Lastly, Piwowarski *et al.*[71] showed that LPBF IN939 exposed to high-temperature solution and aging treatments produced fully equiaxed grains, with HT1 (1,210 °C/8 h + 1,000 °C/6 h + 800 °C/4 h) achieving a UTS of 1,428.5 MPa and a γ' size of ~24.2 μm, while HT2 achieved 134.9 μm and a slightly lower UTS of 1,394.9 MPa. When taken as a whole, these studies highlight how LPBF and SLM naturally encourage columnar cellular microstructures, while solution treatment, HIP, and carefully designed aging schedules control recrystallization behavior, γ' size and volume fraction, and ultimately the tensile strength anisotropy balance in AM IN939.

Table 5. Effects of heat-treatment conditions on tensile properties and microstructural features of additively manufactured IN939

No.	Author	Heat treatment/heat-treatment schedule	Tensile properties (MPa)	γ'/η precipitate size	Grain or cell morphology
1.	Shaikh *et al.*[75]	Aging without solution treatment: 1,000 °C/6 h + 700 °C/16 h	1,429 ± 35	200–300 nm	Spherical γ' precipitates; plate-like features
		Aging with solution treatment: 1,190 °C/4 h + 1,000 °C/6 h + 700 °C/16 h	1,438 ± 10	-	Absence of plate-like feature
2.	Sulak *et al.*[58]	1,160 °C/4 h + 1,000 °C/6 h + 800 °C/4 h	UTS: ~1,050–1,150; YS: ~850–950	0.18 μm	Columnar grains with <001> texture
3.	Gusain *et al.*[59]	HT3 stress relief: 900 °C/4 h + 1,190 °C/4 h + 1,000 °C/6 h + 800 °C/4 h	UTS: ~1,200; YS: ~900	Primary γ': 205 nm; secondary γ': 20 nm; mono-/bimodal distribution	Large equiaxed grains
4.	Maly *et al.*[60]	As-built condition with room temperature–400 °C preheating	UTS: ~1,250	Not reported	Wider columnar grains; larger melt pools
5.	Kumar *et al.*[72]	Direct aging 1:800 ° C/6 h, AC	YS: 1,040 ± 6	25–30 nm	Retained cellular–columnar structure
		Direct aging 2: 1,000 °C/6 h, AC + 800 °C/6 h, AC	YS: 1,235 ± 26	250 nm	η phase present; grain morphology largely retained
		Solution treatment: 1,190 °C/4 h, FC	YS: 930	100–200 nm	γ' coarsening without recrystallization
		Solution treatment: 1,190 °C/4 h, AC	-	50 nm	Slight coarsening of subcellular features
		1,190 °C/4 h, WQ + 1,000 °C/6 h, AC + 800 °C/6 h, AC	930 MPa (room temperature); 630 MPa (816 °C)	80–100 nm	Optimized γ' distribution; no equiaxed recrystallization
		1,190 °C/4 h, AC + 1,000 °C/6 h, AC + 800 °C/6 h, AC	-	80–100 nm	Cellular–columnar morphology retained
		1,190 °C/4 h, FC + 1,000 °C/6 h, AC + 800 °C/6 h, AC	-	250–300 nm	Cellular–columnar morphology retained
6.	Kumar *et al.*[83]	Solution treatment: 1,190 °C/4 h + aging: 1,000 °C/6 h + 800 °C/4 h	UTS: 1,403 ± 11 (T); 1,385 ± 4 (L)	80–180 nm	Equiaxed cells
7.	Kanagarajah *et al.*[64]	Solution treatment: 1,160 °C/4 h + aging: 850 °C/16 h	UTS: ~1,150–1,250	35–70 μm	Recrystallized grains; weaker texture after heat treatment
8.	Güler *et al.*[82]	HT1: HIP + aging: 1,190 °C/4 h + 1,000 °C/6 h + 800 °C/4 h	UTS: 760–780	γ' volume fraction: 31.6%	Directional coarsening/plate-like distortion
		HT2: VHT + aging: 1,190 °C/4 h + 1,000 °C/6 h + 800 °C/4 h	UTS: 750–770	γ' volume fraction: 32.1%	Spherical coalescence and partial dissolution
9.	Li *et al.*[62]	HIP: 1,200 °C + 4 h, 120 MPa, FC	1,153 ± 50	-	Homogenized columnar grains
		HIP + heat treatment: 1,140 °C/4 h, AC + 850 °C/18 h, AC	987 ± 116	γ': <200 nm	Homogeneous γ' distribution in columnar grains
10.	Ozer *et al.*[84]	HT1: 1,120 °C/4 h + 1,000 °C/6 h + 800 °C/4 h	Not reported	Primary γ': 2 μm	Coarsened primary γ' phase; plate-like η phase
		HT2: 1,120 °C/4 h + 850 °C/8 h + 750 °C/8 h	Not reported	Primary γ': 70–120 nm; γ' volume fraction: 30.6%	Spherical primary γ' phase
11.	Piwowarski *et al.*[71]	HT1: 1,210 °C/8 h + 1,000 °C/6 h + 800 °C/4 h	UTS: 1,428.5	24.2 μm	Equiaxed grains
		HT2: 1,240 °C/8 h + 1,000 °C/6 h + 800 °C/4 h	UTS: 1,394.9	134.9 μm	Equiaxed grains

Abbreviations: AC: Air cooling; FC: Furnace cooling; HIP: Hot isostatic pressing; HT: Heat treatment; L: Longitudinal direction; T: Transverse direction; UTS: Ultimate tensile strength; VHT: Vacuum heat treatment; WQ: Water quenching; YS: Yield strength; γ': Gamma prime phase; η: Eta phase.

5. Fatigue and creep behavior of IN939

Powder bed fusion has become a viable fabrication route for investigating the fatigue behavior of IN939, from low-cycle fatigue (LCF) to high-cycle fatigue (HCF). The research history of AM-fabricated IN939 has demonstrated better fatigue performance than cast IN939 across LCF, HCF, and thermomechanical fatigue (TMF) regimes, owing to its fine microstructure and higher strength. Kanagarajah *et al.*[64] compared the fatigue life of the as-built and the as-cast samples and reported significantly longer fatigue life for SLM-processed IN939 at room temperature, which was attributed to the microstructural control, precipitate formation, and high yield strength. The aged SLM-processed and as-cast conditions showed lower fatigue lives (number of cycles to failure [N_f]: 209,272) than the corresponding room-temperature as-built condition. At elevated temperatures, lower fatigue life was observed in the SLM-processed built condition, attributed to process-induced defects. The research work carried out on LCF at room temperature by Babinský *et al.*[85] demonstrated that LPBF (N_f: 90,915/strain amplitude: 0.35%) provides better LCF properties compared to cast IN939 samples (N_f: 11,380/strain amplitude: 0.35%). Casting defects and the presence of carbides were the main causes for the lower fatigue life. The effect of specimen orientation on fatigue behavior shows that the horizontal specimen exhibits better properties, due to enhanced precipitation strengthening and a high tensile yield strength. Thermomechanical fatigue study on IN939 revealed that the lifetime depends on the phase relationship between strain, temperature, and build orientation. The TMF behavior of horizontally and vertically built specimens subjected to a three-step heat treatment was investigated at strain amplitudes of 0.3–0.9% across 400–800 °C. Horizontally built exhibited lower fatigue life due to the <001> texture in the build direction. Fatigue crack initiation occurred more rapidly due to the high strain amplitude. These findings indicate that build direction is a key factor controlling stress response and fatigue life.[86] Defect tolerance study in high cycle fatigue reveals the presence of gas pores (sphericity > 0.6), also consisting of lack of fusion (Ferret diameter: 37 μm) defects controlling the fatigue failure. The sharp corners of lack-of-fusion defects significantly affect fatigue life because they act as crack-initiation sites.[87] Fatigue crack growth assessment was examined with respect to horizontal and vertical AM build direction by Shahini *et al.*[88] A slower crack growth rate with a smaller Paris law exponent (m) was observed. The scatter of the exponent was found to be larger in transverse orientation. The two power-law fits in the threshold and Paris-law regimes were resolved quantitatively at the microscale level.

Researchers have also explored the creep behavior (Table 6). Banoth *et al.*[89] studied the effects of recrystallization and heat treatment on the creep behavior of SLM-fabricated IN939 at 816 °C/250 MPa, using cast IN939 as a comparator. The as-built SLM-processed IN939 exhibits extremely low creep life due to high dislocation density and a small grain size (~32 μm, with only 5.75% recrystallisation). During lower temperature heat treatment (LTH), the grain size remained significantly small (~27 μm) with a recrystallization fraction of 12.8%, and the presence of ~44 nm γ' precipitates along with detrimental η-phase at grain boundaries continued to limit creep performance. A significant improvement was observed in higher temperature heat treatment (HTH), where creep life improved 2.7-fold relative to the LTH condition, as the grain size increased (~50 μm) with a higher recrystallization fraction (~66%), reduced dislocation density, and improved γ' morphology. Despite this improvement, the creep resistance of SLM-fabricated IN939 was still lower than that of cast IN939. The coarser grain structure (~200 μm) and complete recrystallization (~99.9%) led to lower creep strain rate and higher creep life, due to reduced grain boundary sliding, stable carbide network, and favorable γ' coarsening during creep exposure. Kumar *et al.*[72] conducted creep tests at 760–816 °C under stresses of 200–300 MPa and showed that the as-built and direct-aged (DA1) conditions, defined by fine γ' precipitates of ~25–30 nm and a retained cellular-columnar structure (~1 μm × 300 nm), exhibited low creep resistance due to high dislocation density and insufficient binding of dislocation motion. DA2 (direct aging) was conducted at a higher temperature; the γ' precipitate became coarser (~250 nm), with the presence of secondary γ' (~20 nm) and the formation of plate-like η-phase (Ni_3Ti). γ' precipitate coarsening improved creep strength; the presence of η-phase introduced lattice incompatibilities and dislocation accumulation at phase boundaries, thereby reducing long-term creep stability. Solution-treated with two steps of aging, which is water quenched (SWQTA), forms an optimal γ' size distribution of ~80–100 nm without significant η-phase formation, which results in improved creep resistance.

6. Mechanistic modeling

Industry-wide adoption of layer-wise manufacturing processes has accelerated due to the increasing need for quick production of reliable, high-quality, and defect-free components. Before a component is released onto the market, it is customary to test it through multiple trial-and-error cycles; however, developing a single prototype can be costly and time-consuming.[1] Therefore, controlling several interdependent factors, including material properties, transient thermal fields, solidification conditions, cooling rates, scanning patterns, hatch spacing, and heat source contact time, is essential for process optimization.[90] Introducing predictive computational methods to assess product performance before manufacturing has helped overcome these obstacles. Before initiating a build, these models can predict geometry, microstructure, mechanical properties, residual stresses, and defects (Figure 4). Because heat transfer and fluid flow significantly impact microstructural development and mechanical response, incorporating these phenomena improves model accuracy. To better understand cooling rates, solidification parameters, microstructural features, porosity, and residual stress, it is essential to combine theoretical and experimental methods, as several studies have shown that simulations and experimental data align well.[90] During manufacturing, complicated thermal histories are produced by the moving heat source's multiple cycles of heating, melting, cooling, and solidification.[91–93] The rapid circulation within the molten pool is driven by Marangoni convection, which transfers heat and generates local temperature variations.[94] Mechanistic models are needed because internal thermal states cannot be measured, even though surface temperature can be measured experimentally. Thus, the size of the fusion zone, temperature fields, grain structure, texture, residual stress, distortion, and defect development are all determined by simulations of heat transfer, fluid movement, and mass transfer.[95] The research scope is vital in defining modeling outcomes. At the microscale, simulations provide insights into solidification, melting, and powder behavior, while at a large scale, the focus is on the global thermal cycle, stress development, and distortion changes. Multiscale modeling helps improve melt-pool stability, powder-bed characterization, and structural performance prediction. Region-specific modeling can provide additional insight into the suitability of different powder morphologies and particle-size distributions.[92,95]

6.1. Heat transfer and fluid flow

Trial-and-error testing has been the conventional way of determining the correct process parameters, but this is time-consuming and expensive with processes such as LPBF.[96–99] A sufficient substitute is provided by numerical simulations, which use three-dimensional heat transfer and fluid flow models to predict intermediate temperature profiles, velocity profiles, cooling rates, solidification, and the overall build geometry. These properties are temperature-dependent and depend on variables such as size distribution, packing efficiency, absorptivity, powder thermal conductivity, and shielding gas composition.[100] Surface-tension gradients at the liquid–gas interface drive convection within the molten pool. The flow of such thermocapillary forces can result in highly nonlinear fluid behavior and is a limiting factor in heat transfer. Thus, to recreate experimental results, it is critical to properly incorporate the size of the powder particles, their distribution, and other micro-scale characteristics.[101,102]

Mass, momentum, and energy conservation govern heat transfer and fluid flow in the molten pool. The governing equations are expressed as follows[103]:

(a) Continuity equation:

$$\frac{\partial(\rho u_i)}{\partial x_i} = 0 \tag{2}$$

(b) Momentum equation:

$$\frac{\partial(\rho u_j)}{\partial t} + \frac{\partial(\rho u_i u_j)}{\partial x_i} = \frac{\partial}{\partial x_i}\left(\mu \frac{\partial u_j}{\partial x_i}\right) + S_{uj} - K_P \frac{(1-f_L)^2}{\left(f_L^3 + B_N\right)} u_j \tag{3}$$

(c) Energy equation[104]:

$$\rho \frac{\partial h}{\partial t} + \frac{\partial(\rho u_i h)}{\partial x_i} = \frac{\partial}{\partial x_i}\left(\left(\frac{k}{C_p}\right)\frac{\partial h}{\partial x_i}\right) - \rho \frac{\partial \Delta H}{\partial t} - \rho \frac{\partial(u_i \Delta H)}{\partial x_i} + S_h \tag{4}$$

6.2. Marangoni force

Marangoni flow is the movement of molten metal on the surface of a pool due to temperature-dependent variations in surface tension. It is primarily driven by surface-tension gradients, which strongly influence the dynamics of melt pools.[105] In pure metals, surface tension generally decreases with increasing temperature, so molten metal tends to flow from hotter, lower-surface-tension regions toward cooler, higher-surface-tension regions. In addition to enhancing the convective heat transfer, this flow is also necessary to form the melt pool.[105] The case is, however, more complicated with multicomponent alloys. Elements such as sulfur and selenium can have a significant effect on the response of surface tension to temperature and may even reverse the direction of flow.[104] Gradients in temperature and composition affect surface tension in Ni-based superalloys.[95] The concept of Marangoni convection is a crucial aspect of LPBF modeling, as it directly affects the shape of the fusion zone, microstructural refinement, and defect susceptibility.[104] The shapes of the fusion zone, chemical composition, thermal history, temperature gradients, and solidification rates are all factors that affect the microstructural characteristics and defects, which, in turn, determine the performance and properties of additively manufactured materials. It may be difficult to comprehend these factors in depth solely through experimental methods, and this may take a long time.

Table 6. Creep behavior of IN939

Factor	Kumar *et al.* (2025)	Banoth *et al.* (2020)
Creep condition	SWQTA: 11.5 h at 816 °C/300 MPa	HTH: 554 h at 816 °C/250 MPa
Creep mechanism	Dislocation climb (n = 4.2, Q = 480 kJ/mol)	Recrystallization-driven grain-boundary fracture
η phase	Present in DA2 → reduces creep, ductility	Present in LTH → reduces creep life
Grain size effect	Smaller grains → higher minimum creep strain rate	Significant during creep → beneficial in HTH and cast

Abbreviations: DA2: Direct aging 2; HTH: High-temperature heat treatment; LTH: Low-temperature heat treatment; SWQTA: Solution treatment followed by water quenching and two-step aging.

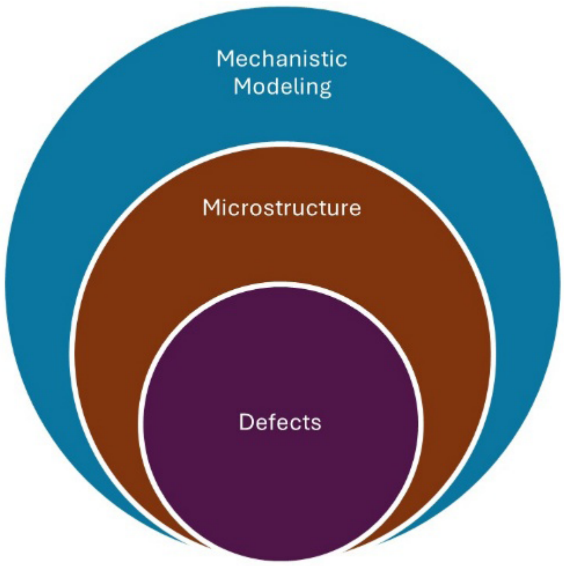

Figure 4. Mechanistic modeling in the prediction of microstructure and defects

Thus, mechanistic modeling has become a useful tool for incorporating these factors to predict material behavior and generate valid outcomes.[94]

6.3. Effect of thermal history on microstructural evolution

Additive manufacturing involves depositing one layer on top of the previous layer, resulting in steeper temperature gradients and cooling rates, and thus the microstructure of additively manufactured materials is quite different from that of traditionally manufactured materials. Changes in process parameters have a direct effect on the development of the microstructure and mechanical properties compared to cast materials. Thus, it is necessary to know them and how they relate to one another. The Hall–Petch relation helps explain the strength increase associated with grain refinement, whereby smaller grains can impede dislocation motion more effectively. The variations of the microstructure can be regulated primarily by processing factors, and the time-temperature history has a major role.[104] Conditions of solidification, i.e., the cooling rate and flow direction of the molten metal, are key factors in the development of the microstructure. Yet, these properties are difficult to determine experimentally because their dynamic range is very high and the time spent in the molten state is very short. Mechanistic modeling is also crucial in such studies since it allows for predicting the solidification behavior and gives the parameters needed to design and control the desired microstructure of the build.[101,106–109]

6.3.1. Solidification morphologies

Solidification conditions strongly influence functional performance, and tensile properties are largely determined by grain morphology and size, including whether the grains are columnar or equiaxed. Elongated columnar grains are especially advantageous to LPBF, because they reduce the process of initiation and propagation of cracks caused by hot tearing.[110,111]

Mechanistic modeling has become an important tool for understanding the challenges of LPBF of IN939, a Ni-based superalloy strengthened by γ' precipitates. Recent modeling studies have considered the coupled thermal, microstructural, and mechanical processes that dominate defect development and performance in AM-fabricated IN939. At the solidification and microstructure level, physics-based models all emphasize the non-equilibrium character of LPBF processing. Intensive melt convection, as shown by fully coupled thermal-fluid-solute-microstructure simulations, has been used to explain the mechanism of how solute redistribution at the solid-liquid interface can switch between ultra-fine cellular structures to coarser cells and how accelerated solidification can potentially reduce the cracking susceptibility by reducing solute enrichment in the inter-dendritic region.[112]

Computational thermodynamics predicts the formation of a low-melting residual liquid enriched in carbon, boron, and zirconium at high solid fractions, which can be considered the main cause of solidification cracking. These models have proven useful in alloy design by guiding alloy modification strategies that reduce the stability of residual liquid films and allow crack-free AM IN939 builds, e.g., by adding Si.[113] A process–microstructure–property approach based on finite-element thermal modeling, phase-field simulations, and CALPHAD methods can provide quantitative predictions of the connection between the thermal histories of LPBF, patterns of micro segregation, and the formation of secondary phases.[114]

Although these models are commonly exemplified at related Ni-based superalloys, they are directly applicable to IN939, providing a mechanistic understanding of γ' precipitation, carbide formation, and thermodynamic driving forces of deleterious phases during post-processing heat treatments. At the mechanical and constitutive modeling scale, the orientation- and temperature-dependent responses of AM Ni-based superalloys are described using anisotropic elasto-plastic models, calibrated using cyclic loading measurements. The modified Ohno–Wang constitutive formulations are based on transversely isotropic materials and successfully capture mid-life cyclic behavior, plastic strain ranges, and hysteresis responses, which are crucial inputs for fatigue life prediction of AM components.[115]

The models provide a strong mechanistic framework for 3D printing. Therefore, the combination of experimental work and prediction, using cracking and creep mechanisms, describes the performance constraints in AM-fabricated IN939. Recrystallization-controlled creep models indicate that dislocation density, grain structure, size of the γ' precipitate, and grain-boundary phase stability all combine to determine high-temperature deformation and rupture behavior. Solution treatment is mechanistically proven to increase the proportion of recrystallized grains with lower dislocation density and remove deleterious η phases.[89] Simultaneously, composition-based models of cracking separate solidification from solid-state cracking and emphasize the importance of the solidification range, stress relaxation, and ductility dip behavior.[116]

6.4. Defects

Mechanistic modeling offers a viable approach to defining the variables in processes that impact defect formation and to predicting the nature of defects likely to arise in manufacturing. This kind of modeling goes along with processes for minimizing or removing defects in additively produced materials, in addition to helping with prediction. The defects that have a major bearing on the overall performance and structural integrity of the end product are solidification cracking, alloying elements lost through vaporization, lack-of-fusion porosity, formation of residual stress, and deformation.[104]

6.4.1. Vaporization

Alloying elements in the molten pool, which vaporize at high processing temperatures, can alter the composition of alloys produced by AM. It is especially noticeable in electron beam-based processes, in which the element evaporation is hastened by the joint effect of high temperatures and low pressure in the chamber.[117–119] Since each alloying element vaporizes at a different rate, localized compositional changes can influence the material's microstructure and properties. In LPBF, heat transfer and fluid flow models are essential for predicting such elemental losses. Accurately calculating temperature variations at the molten surface is necessary to determine vaporization rates and reduce compositional deviations during processing.[94]

6.4.2. Spattering

Spattering is a common LPBF defect that generally occurs in two forms: the displacement of powder particles along the melt track and the ejection of liquid droplets from the molten pool.[120–123]

(a) Ejection of liquid metal droplets

On the liquid surface of the molten pool, intense vaporization at high temperatures generates a rebound pressure. When this recoil force exceeds the stabilizing effect of surface tension[124], the molten droplets are ejected from the pool. In addition to increasing surface roughness and porosity, the ejection of these droplets also affects powder distribution, undermining the stability and uniformity of subsequent layers.

(b) Ejection of powder particles

A rapidly moving vapor jet forms due to intense evaporation in the molten pool during LPBF. This vapor jet creates a small low-pressure zone caused by inward gas flow, explained by the Bernoulli effect.[125] This inward flow, controlled by the scanning path and laser material contact point, predominantly influences the amount of particle ejection.[122] Additionally, limited laser melting conditions at a specific site enhance the combined effects of particle excitation, shielding gas flow, and vapor jet formation.[126] The timescales for these processes are very short: material melting occurs within a few microseconds, vapor jet formation takes about 10 ms, and argon gas flow develops over roughly 100 ms.[126]

6.4.3. Voids/Porosity

Pore formation is one of the most common flaws observed in materials produced by AM. Insufficient fusing between neighboring tracks, unstable keyhole collapse, and gas trapping leading to residual porosity frequently cause pore development.[127]

(a) Unmelted powder/Lack of fusion

When there is insufficient overlap between neighboring deposited tracks, proper bonding is prevented, leading to a lack of fusion defects. This occurs due to various factors, such as excessively high scanning rates, inadequate laser power, and thicker layers, all of which hinder full melting and cause lack-of-fusion defects.[128,129] If hatch spacing is too large, voids may form in inter-track regions, leading to uneven heating and partial melting of the feedstock. The issue can be aggravated by process instability, which may also change the size and depth of the molten pool. Sound metallurgical bonding mainly depends on the spatial arrangement of successive tracks and layers, but inadequate feedstock delivery, faulty powder packing, and vapor-driven ejection of restricted powder particles can also contribute to the absence of fusion defects.[120,125]

(b) Keyhole-induced porosity

High laser power and scanning rates in AM are the main causes of keyhole porosity, resulting in a fusion zone with a high depth-to-width ratio. Due to the partial remelting of underlying layers caused by this concentrated energy input, voids may form, migrate upward within the melt pool, and become trapped during solidification.[130]

(c) Gas-induced porosity

Gas-induced porosity, which is commonly characterized by tiny, spherical pores, is another prevalent flaw in LPBF.[131,132] The residual gases trapped during feedstock production are the source of these pores.[133] Gases dissolved in the molten pool or in pre-existing pores from earlier processing stages escape during solidification, creating voids.[130] For example, powder atomization creates tiny gaps inside particles that may come together during processing. Within the melt pool, these trapped bubbles may expand, merge with larger holes, and persist through multiple build layers.[134] Furthermore, gas trapping caused by spatter during LPBF might promote pore formation. Over time, these processes develop larger and more harmful porosity characteristics in the manufactured part.[129]

6.5. Cracking in additive manufacturing

One of the most common flaws observed in metallic alloy AM is cracking. Three primary types of cracks are frequently found in Ni-based superalloys: ductility dip cracking (DDC), liquation cracking, and solidification cracking.[117,133,135]

6.5.1. Solidification cracking

Hot cracking, also known as solidification cracking, is a common issue in additively produced Ni-based alloys. It results from high solidification shrinkage rates caused by rapid cooling. Cracks initiate and propagate along the weak interdendritic regions of the solidifying material when tensile stresses exceed its yield strength. The solid fraction versus temperature and the alloy's solidification range significantly influence its susceptibility to solidification cracking.[136–143]

6.5.2. Liquation cracking

Liquation cracking is another major flaw found in AM-produced Ni alloys. It begins at partially melted areas near the fusion line, where liquid layers form grain boundaries. The forces generated by thermal contraction cause these weakened grain boundaries to break. When low-melting-point liquid phases are present, cracks can extend across interdendritic regions, previously deposited layers, and overlapping tracks, worsening this issue.[144,145]

6.5.3. Ductility dip cracking

Nickel-based superalloys and other FCC alloys are the primary targets of DDC, a solid-state cracking phenomenon.[146] The DDC process does not require liquid films, unlike liquation cracking. Localized ductility generally decreases significantly within a critical temperature range, roughly half the melting point to the recrystallization temperature.[143,147] Grain boundary precipitates, local tensile stresses, grain boundary deformation, and grain size effects increase DDC, which is often intergranular. The combined effect of these factors determines how susceptible additively manufactured components are to DDC.[143,147]

6.6. Surface roughness in additive manufacturing

Surface roughness also significantly affects the dimensional accuracy and geometric tolerances of products made through AM. Some causes of poor surface quality include near-surface cavities and voids[148], the staircase effect resulting from irregular transitions between adjacent tracks and layers[129], and spatter deposits on the part surface.[149] Other contributing factors are partially bonded particles at the edges of the melt pool and melt pool instabilities.[150,151] These combined processes deteriorate surface quality, often requiring extensive post-processing.

7. Conclusion

The review addresses AM routes for processing IN939, with emphasis on microstructure, defects, heat treatment, and mechanical properties. The demand for components capable of operating at high service temperatures has increased interest in AM techniques for Ni-based superalloys. The primary powder bed fusion processes used to print IN939 overcome the limitations of traditional methods (casting/forging). A comparison of the strength of complex-geometry components fabricated via LPBF, DED, and EBM provides insights into the existing literature on microstructural behavior along the build direction. Optimization of processing parameters while adopting the fabrication method impacts the size distribution of formed precipitate (γ'). Microstructural evolution dependent on build orientation showed that IN939 possesses melt pool boundaries as its characteristic feature, validating the AM process. By correlating morphology and thermal history with mechanistic modeling, the studies revealed that thermodynamic parameters also play a vital role. Heat transfer, fluid flow, and Marangoni forces (surface tension) are among the major predictive parameters in mechanistic modeling, which affect the melt pool structure. The effect of the alloying elements in this series enables this material to operate at high temperatures. The Co percentage determines its crack susceptibility, whereas the sulfur content determines the depth and width of the melt pool. The transition in microstructure (grain morphology) from planar-cellular-columnar to equiaxed depends on the solidification rate and thermal gradient.

Furthermore, this article provides a brief summary of the effects of post-processing methods investigated by renowned researchers. According to the time-temperature phase diagram, the strength can reach up to 1,500 MPa. Solutionizing and aging studies are adopted to remove the unwanted secondary phases present and the residual stresses introduced during building. HIP is one technique for reducing porosity and increasing specimen density. The temperature range for HIP is usually 1,150–1,160 °C/4 h (pressure:100–150 MPa). Importantly, mechanical performance with respect to high-temperature studies, heat treatment, and room temperature, in accordance with build orientation, indicates that the thermal history affects the material's load-bearing capacity. Limited studies on IN939's creep and fatigue behavior necessitate exploring this at an advanced level (high-temperature fatigue/creep).

Despite recent advances, defect formation remains a key issue during the AM of IN939 components. The variants of the cracking mechanism (solidification, liquation, ductility dip) are all correlated with thermal conditions, spattering, and porosity, thereby affecting density.

To further enable the reliable use of additively manufactured IN939 in challenging service environments, future research should focus on adopting mechanistic modeling with experimental validation to predict corrosion and fatigue degradation behavior.

Acknowledgments

None.

Funding

The authors would like to acknowledge Vellore Institute of Technology, Vellore, for providing support for the open-access publication of this article.

Conflict of interest

The authors declare that no conflict of interest exists in this work.

Author contributions

Conceptualization: Raja Annamalai
Data curation: Pranjal Singh, Sheeza Khan
Formal analysis: Pranjal Singh, Sheeza Khan
Investigation: Sheeza Khan
Methodology: Sheeza Khan
Supervision: Raja Annamalai
Visualization: Raja Annamalai
Writing–original draft: Pranjal Singh, Sheeza Khan
Writing–review & editing: Sheeza Khan, Raja Annamalai

Ethics approval and consent to participate

Not applicable.

Consent for publication

Not applicable.

Availability of data

Not applicable.

References

1. Debroy T, Wei HL, Zuback JS, *et al.* Additive manufacturing of metallic components: process, structure, and properties. *Prog Mater Sci.* 2018;92:112-224.

   doi: 10.1016/j.pmatsci.2017.10.001

2. Herzog D, Seyda V, Wycisk E, Emmelmann C. Additive manufacturing of metals. *Acta Mater*. 2016;117:371-392.

   doi: 10.1016/j.actamat.2016.07.019

3. Clare AT, Mishra RS, Merklein M, *et al.* Alloy design and adaptation for additive manufacture. *J Mater Process Technol.* 2022;299:117358.

   doi: 10.1016/j.jmatprotec.2021.117358

4. Kumar V, Ravi MU, Naik Y. A review paper on Inconel alloys. *Int J Adv Eng Manag.* 2022;4(8):566-573.

   doi: 10.35629/5252-0408566573

5. Zupanič F, Bončina T, Križman A, Tichelaar FD. Structure of continuously cast Ni-based superalloy Inconel 713C. *J Alloy Compd.* 2001;329(1-2):290-297.

   doi: 10.1016/S0925-8388(01)01676-0

6. Solitaire Overseas. What is Inconel 600 and its uses? Available from: https://www.solitaire-overseas.com/blog/what-is-inconel-600-and-its-uses [Last accessed on October 23, 2025].

7. Fu S, Dong J, Zhang M, Wang N, Xie X. Research on Inconel 718 Type Alloys with Improvement of Temperature Capability. In: *Superalloy 718 and Derivatives*. Wiley; 2010:281-296.

   doi: 10.1002/9781118495223.ch21

8. Shoemaker LE. Alloys 625 and 725: trends in properties and applications. In: Reichman S, Duhl DN, Maurer G, Antolovich S, Lund C, eds. *Superalloys 1988*. The Minerals, Metals & Materials Society; 1988:409-418.

   doi: 10.7449/1988/Superalloys_1988_409_418

9. Herchenroeder RB. "HAYNES" alloy No. 188 aging characteristics. In: Avery DH, Harris SJ, eds. *Superalloys 1968*. The Metallurgical Society of AIME; 1968:460-500.

   doi: 10.7449/1968/Superalloys_1968_460_500

10. Machine MFG. Inconel X750 (UNS N07750) composition, properties, and applications. Available from: https://shop.machinemfg.com/inconel-x750-uns-n07750-composition-properties-and-applications/.[Last accessed on October 23, 2025].

11. Amirian B, Asad A, Krezan L, Yakout M, Hogan JD. A new perspective on the mechanical behavior of Inconel 617 at elevated temperatures for small modular reactors. *Scr Mater*. 2025;261:116605.

    doi: 10.1016/j.scriptamat.2025.116605

12. Langley Alloys. Discover more about Incoloy 925. Available from: https://www.langleyalloys.com/blog/discover-more-about-incoloy-925 [Last accessed on October 23, 2025].

13. Haynes International. Our heritage: Our milestones. Available from: https://haynesintl.com/en/our-company/our-heritage/our-milestones [Last accessed on October 23, 2025].

14. Special Metals Corporation. INCONEL® alloy 751. Available from: https://www.specialmetals.com/documents/technical-bulletins/inconel/inconel-alloy-751.pdf [Last accessed on October 23, 2025].

15. Shahwaz M, Dogu MN, Gu H, Brabazon D, Sen I. Microstructural evolution and mechanical behavior of additively manufactured IN939 superalloy at room and elevated temperatures. *J Alloys Compd*. 2026;1050:185949.

    doi: 10.1016/j.jallcom.2026.185949

16. De Lorenzi Mariana S, Soh V, Wuu D, *et al.* Innovations in IN939: From Cast Alloy to Additive Manufacturing. *High-Temp Mater.* 2025;2(1):10003.

    doi: 10.70322/htm.2025.10003

17. Sames WJ, Unocic KA, Dehoff RR, Lolla T, Babu SS. Thermal effects on microstructural heterogeneity of Inconel 718 materials fabricated by electron beam melting. *J Mater Res*. 2014;29(17):1920-1930.

    doi: 10.1557/jmr.2014.140

18. Sun SH, Koizumi Y, Saito T, *et al.* Electron beam additive manufacturing of Inconel 718 alloy rods: Impact of build direction on microstructure and high-temperature tensile properties. *Addit Manuf*. 2018;23:457-470.

    doi: 10.1016/j.addma.2018.08.017

19. Balachandramurthi AR, Moverare J, Mahade S, Pederson R. Additive manufacturing of alloy 718 via electron beam melting: Effect of post-treatment on the microstructure and the mechanical properties. *Materials*. 2018;12(1):68.

    doi: 10.3390/ma12010068

20. Cordero PM, Mireles J, Ridwan S, Wicker RB. Evaluation of monitoring methods for electron beam melting powder bed fusion additive manufacturing technology. *Prog Addit Manuf.* 2017;2(1-2):1-10.

    doi: 10.1007/s40964-016-0015-6

21. Raghavan N, Simunovic S, Dehoff RR, *et al*. Localized melt-scan strategy for site specific control of grain size and primary dendrite arm spacing in electron beam additive manufacturing. *Acta Mater*. 2017;140:375-387.

    doi: 10.1016/j.actamat.2017.08.038.

22. Zhu J, Wise A, Nuhfer T, *et al*. High-temperature-oxidation-induced ordered structure in Inconel 939 superalloy exposed to oxy-combustion environments. *Mater Sci Eng A*. 2013;566:134-142.

    doi: 10.1016/j.msea.2012.12.074.

23. Shaikh AS. Development of a γ′ Precipitation Hardening Ni-Base Superalloy for Additive Manufacturing [master's thesis]. Gothenburg, Sweden: Chalmers University of Technology; 2018.

    doi: 10.13140/RG.2.2.11472.81921

24. Marchese G, Parizia S, Saboori A, *et al.* The influence of the process parameters on the densification and microstructure development of laser powder bed fused inconel 939. *Metals*. 2020;10(7):882.

    doi: 10.3390/met10070882

25. Zhang B, Ding H, Meng AC, Nemati S, Guo S, Meng WJ. Crack reduction in Inconel 939 with Si addition processed by laser powder bed fusion additive manufacturing. *Addit Manuf*. 2023;72:103623.

    doi: 10.1016/j.addma.2023.103623

26. Dejene ND, Lemu HG. Current Status and Challenges of Powder Bed Fusion-Based Metal Additive Manufacturing: Literature Review. *Metals*. 2023;13(2).

    doi: 10.3390/met13020424

27. Guo C, Li S, Shi S, *et al.* Effect of processing parameters on surface roughness, porosity and cracking of as-built IN738LC parts fabricated by laser powder bed fusion. *J Mater Process Technol*. 2020;285:116788.

    doi: 10.1016/j.jmatprotec.2020.116788

28. Sukumaran A, Gupta RK, Anil Kumar V. Effect of Heat Treatment Parameters on the Microstructure and Properties of Inconel-625 Superalloy. *J Mater Eng Perform*. 2017;26(7):3048-3057.

    doi: 10.1007/s11665-017-2774-8

29. Li C, White R, Fang XY, Weaver M, Guo YB. Microstructure evolution characteristics of Inconel 625 alloy from selective laser melting to heat treatment. *Mater Sci Eng A*. 2017;705:20-31.

    doi: 10.1016/j.msea.2017.08.058

30. Xu J, Kontis P, Peng RL, Moverare J. Modelling of additive manufacturability of nickel-based superalloys for laser powder bed fusion. *Acta Mater*. 2022;240:118307.

    doi: 10.1016/j.actamat.2022.118307

31. Murr LE, Gaytan SM. Electron Beam Melting. In: *Comprehensive Materials Processing*. Elsevier; 2014:135-161.

    doi: 10.1016/B978-0-08-096532-1.01004-9

32. Bansal SA, Khanna V, Gupta P. *Metal Matrix Composites*. CRC Press; 2022.

    doi: 10.1201/9781003194897

33. Volpato GM, Tetzlaff U, Fredel MC. A comprehensive literature review on laser powder bed fusion of Inconel superalloys. *Addit Manuf*. 2022;55:102871.

    doi: 10.1016/j.addma.2022.102871

34. Reed RC. *The Superalloys: Fundamentals and Applications*. Cambridge University Press; 2008.

    doi: 10.1017/CBO9780511541285

35. Wang X, Gong X, Chou K. Review on powder-bed laser additive manufacturing of Inconel 718 parts. *Proc Inst Mech Eng B J Eng Manuf*. 2017;231(11):1890-1903.

    doi: 10.1177/0954405415619883

36. Zhao Y, Guo Q, Ma Z, Yu L. Comparative study on the microstructure evolution of selective laser melted and wrought IN718 superalloy during subsequent heat treatment process and its effect on mechanical properties. *Mater Sci Eng A*. 2020;791:139735.

    doi: 10.1016/j.msea.2020.139735

37. Feng Q, Wu Y, Li J, *et al.* Effects of intermediate temperature on the grain boundary and γ' precipitates of nickel-based powder superalloy under interrupted cooling. *J Alloy Compd.* 2022;922:166310.

    doi: 10.1016/j.jallcom.2022.166310

38. Xu J, Li L, Liu X, Li H, Feng Q. Quantitative models of high temperature creep microstructure-property correlation of a nickel-based single crystal superalloy with physical and statistical features. *J Mater Res Technol.* 2022;19:2301-2313.

    doi: 10.1016/j.jmrt.2022.06.011

39. Gudivada G, Pandey AK. Recent developments in nickel-based superalloys for gas turbine applications: Review. *J Alloy Compd*. 2023;963:171128.

    doi: 10.1016/j.jallcom.2023.171128

40. Hosseini E, Popovich VA. A review of mechanical properties of additively manufactured Inconel 718. *Addit Manuf*. 2019;30:100877.

    doi: 10.1016/j.addma.2019.100877

41. Shahwaz M, Nath P, Sen I. A critical review on the microstructure and mechanical properties correlation of additively manufactured nickel-based superalloys. *J Alloy Compd*. 2022;907:164530.

    doi: 10.1016/j.jallcom.2022.164530

42. Lee D, Park S, Lee CH, *et al.* Correlation between

microstructure and mechanical properties in additively manufactured Inconel 718 superalloys with low and high electron beam currents. *J Mater Res Technol.* 2024;28:2410-2419.

doi: 10.1016/j.jmrt.2023.12.184

43. Teng Q, Xie Y, Sun S, *et al.* Understanding on processing temperature-metallographic microstructure-tensile property relationships of third-generation nickel-based superalloy WZ-A3 prepared by hot isostatic pressing. *J Alloy. Compd*. 2022;909:164668.

doi: 10.1016/j.jallcom.2022.164668

44. Mostafaei A, Ghiaasiaan R, Ho IT, *et al.* Additive manufacturing of nickel-based superalloys: A state-of-the-art review on process-structure-defect-property relationship. *Prog Mater Sci*. 2023;136:101108.

doi: 10.1016/j.pmatsci.2023.101108

45. Sadeghi E, Karimi P, Esmaeilizadeh R, *et al.* A state-of-the-art review on fatigue performance of powder bed fusion-built alloy 718. *Prog Mater Sci*. 2023;133:101066.

doi: 10.1016/j.pmatsci.2022.101066

46. Nowotnik A. Nickel-Based Superalloys. In: *Reference Module in Materials Science and Materials Engineering*. Elsevier; 2016.

doi: 10.1016/b978-0-12-803581-8.02574-1

47. Kontis P, Yusof HAM, Pedrazzini S, *et al.* On the effect of boron on grain boundary character in a new polycrystalline superalloy. *Acta Mater*. 2016;103:688-699.

doi: 10.1016/j.actamat.2015.10.006

48. Deng D, Peng RL, Brodin H, Moverare J. Microstructure and mechanical properties of Inconel 718 produced by selective laser melting: Sample orientation dependence and effects of post heat treatments. *Mater Sci Eng A*. 2018;713:294-306.

doi: 10.1016/j.msea.2017.12.043

49. Sonar T, Balasubramanian V, Malarvizhi S, Venkateswaran T, Sivakumar D. An overview on welding of Inconel 718 alloy - Effect of welding processes on microstructural evolution and mechanical properties of joints. *Mater Charact*. 2021;174:110997.

doi: 10.1016/j.matchar.2021.110997

50. Schwartz M, Gheorghe D, Ciocoiu R. Failure of an Inconel 718 Die used in Production of Hot Copper Direct Extrusion. *J Mater Sci Eng.* 2015;04(06).

doi: 10.4172/2169-0022.1000205

51. Popovich VA, Borisov E V., Popovich AA, Sufiiarov VS, Masaylo D V., Alzina L. Impact of heat treatment on mechanical behaviour of Inconel 718 processed with tailored microstructure by selective laser melting. *Mater Des*. 2017;131:12-22.

doi: 10.1016/j.matdes.2017.05.065

52. Ghorbanpour S, Deshmukh K, Sahu S, *et al.* Additive manufacturing of functionally graded inconel 718: Effect of heat treatment and building orientation on microstructure and fatigue behaviour. *J Mater Process Technol*. 2022;306:117573.

doi: 10.1016/j.jmatprotec.2022.117573

53. Sanchez S, Gaspard G, Hyde CJ, Ashcroft IA, Ravi GA, Clare AT. The creep behaviour of nickel alloy 718 manufactured by laser powder bed fusion. *Mater Des*. 2021;204:109647.

doi: 10.1016/j.matdes.2021.109647

54. Wu Y, Li C, Xia X, Liang H, Qi Q, Liu Y. Precipitate coarsening and its effects on the hot deformation behavior of the recently developed γ'-strengthened superalloys. *J Mater Sci Technol*. 2021;67:95-104.

doi: 10.1016/j.jmst.2020.06.025

55. MacKay RA, Gabb TP, Garg A, Rogers RB, Nathal M V. Influence of composition on microstructural parameters of single crystal nickel-base superalloys. *Mater Charact*. 2012;70:83-100.

doi: 10.1016/j.matchar.2012.05.001

56. Fardan A, Klement U, Brodin H, Hryha E. Effect of Part Thickness and Build Angle on the Microstructure, Surface Roughness, and Mechanical Properties of Additively Manufactured IN-939. *Metall Mater Trans A Phys Metall Mater Sci*. 2023;54(5):1792-1807.

doi: 10.1007/s11661-022-06940-7

57. Zou T, Liu M, Cai Y, *et al.* Effect of temperature on tensile behavior, fracture morphology, and deformation mechanisms of Nickel-based additive manufacturing 939 superalloy. *J Alloy Compd*. 2023;959:170559.

doi: 10.1016/j.jallcom.2023.170559

58. Šulák I, Babinský T, Chlupová A, Milovanović A, Náhlík L. Effect of building direction and heat treatment on mechanical properties of Inconel 939 prepared by additive manufacturing. *J Mech Sci Technol.* 2023;37(3):1071-1076.

doi: 10.1007/s12206-022-2101-7

59. Gusain R, Soleimani Dodaran M, Gradl PR, Shamsaei N, Shao S. The influence of heat treatments on the microstructure and tensile properties of additively manufactured Inconel 939. In: *Solid Freeform Fabrication 2023: Proceedings of the 34th Annual International Solid Freeform Fabrication Symposium – An Additive Manufacturing Conference.* University of Texas at Austin; 2023:598-606.

doi: 10.26153/tsw/50976

60. Malý M, Nopová K, Klakurková L, Adam O, Pantělejev L, Koutný D. Effect of Preheating on the Residual Stress and Material Properties of Inconel 939 Processed by Laser Powder Bed Fusion. *Materials*. 2022;15(18):6360.

doi: 10.3390/ma15186360

61. Zhou X, Liu X, Zhang D, Shen Z, Liu W. Balling phenomena in selective laser melted tungsten. *J Mater Process Technol.* 2015;222:33-42.

doi: 10.1016/j.jmatprotec.2015.02.032

62. Li Y, Liang X, Yu Y, Li H, Kan W, Lin F. Microstructures and mechanical properties evolution of IN939 alloy during electron beam selective melting process. *J Alloy. Compd.* 2021;883:160934.

doi: 10.1016/j.jallcom.2021.160934

63. Philpott W, Jepson MAE, Thomson RC. Comparison of the effects of conventional heat treatments on cast and selective laser melted IN939 alloy. In: Parker J, Shingledecker J, Siefert J, eds. *Advances in Materials Technology for Fossil Power Plants*. Vol 84673. ASM International; 2016:735-746.

doi: 10.31399/asm.cp.am-epri-2016p0735

64. Kanagarajah P, Brenne F, Niendorf T, Maier HJ. Inconel 939 processed by selective laser melting: Effect of microstructure and temperature on the mechanical properties under static and cyclic loading. *Mater Sci Eng A*. 2013;588:188-195.

doi: 10.1016/j.msea.2013.09.025

65. Hanzl P, Zetek M, Bakša T, Kroupa T. The influence of processing parameters on the mechanical properties of SLM parts. *Procedia Eng.* 2015;100:1405-1413.

doi: 10.1016/j.proeng.2015.01.510

66. Ozaner OC, Dursun G, Akbulut G. Effects of wire-EDM parameters on the surface integrity and mechanical characteristics of additively manufactured Inconel 939. *Mater Today Proc.* 2021;38:1861-1865.

doi: 10.1016/j.matpr.2020.08.486

67. Li L, Guo YB, Wei XT, Li W. Surface integrity characteristics in wire-EDM of inconel 718 at different discharge energy. *Procedia CIRP*. 2013;6:220-225.

doi: 10.1016/j.procir.2013.03.046

68. Xavior M A, Ashwath P. Fatigue life and fracture morphology of Inconel 718 machined by spark EDM process. *Procedia Manuf.* 2019;30:292-299.

doi: 10.1016/j.promfg.2019.02.042

69. Subrahmanyam M, Nancharaiah T. Optimization of process parameters in wire-cut EDM of Inconel 625 using Taguchi's approach. *Materials Today: Proceedings*. 2020;23:642-646.

doi: 10.1016/j.matpr.2019.05.449

70. Hibino S, Fujimitsu K, Azuma M, Ishimoto T, Nakano T. Effects of Recrystallization on Tensile Anisotropic Properties for IN738LC Fabricated by Laser Powder Bed Fusion. *Crystals*. 2022;12(6):842.

doi: 10.3390/cryst12060842

71. Piwowarski P, Moszczyńska D, Paradowski K, Wieczorek-Czarnocka M, Mizera J. Influence of Solution Treatment Temperatures on LPBF-Produced Inconel 939 Alloy on Mechanical Performance. *Appl Sci.* 2024;14(21):9625.

doi: 10.3390/app14219625

72. Kumar C, Reddy S, Eswaramoorthy NK, *et al.* Microstructure optimization for improving creep resistance of additively manufactured Ni-based superalloy IN939 through heat treatment. *J Mater Sci*. 2025;60(3):1545-1560.

doi: 10.1007/s10853-024-10337-9

73. Kumar C, Kumar P. Analyzing dynamic strain aging and yield strength anomaly in IN740H, a nickel-based superalloy comprising low volume fraction of γ′. *Materialia*. 2024;33:102028.

doi: 10.1016/j.mtla.2024.102028

74. Pavan AHV, Narayan RL, Li SH, Singh K, Ramamurty U. Mechanical behavior and dynamic strain ageing in Haynes®282 superalloy subjected to accelerated ageing. *Mater Sci Eng A*. 2022;832:142486.

doi: 10.1016/j.msea.2021.142486

75. Shaikh AS, Rashidi M, Minet-Lallemand K, Hryha E. On as-built microstructure and necessity of solution treatment in additively manufactured Inconel 939. *Powder Metall.* 2023;66(1):3-11.

doi: 10.1080/00325899.2022.2041787

76. Visibile A, Gunduz KO, Sattari M, Fedorova I, Halvarsson M, Froitzheim J. High temperature oxidation of inconel 939 produced by additive manufacturing. *Corros Sci*. 2024;233:112067.

doi: 10.1016/j.corsci.2024.112067

77. Rodríguez-Barber I, Fernández-Blanco AM, Unanue-Arruti I, Madariaga-Rodríguez I, Milenkovic S, Pérez-Prado MT. Laser powder bed fusion of the Ni superalloy Inconel 939 using pulsed wave emission. *Mater Sci Eng A*. 2023;870:144864.

doi: 10.1016/j.msea.2023.144864

78. University of Wisconsin–Madison. Types of unit cells: body-centered cubic and face-centered cubic (M11Q5). Chemistry 103 – Minimally Guided General Chemistry. Available from: https://wisc.pb.unizin.org/minimisgenchem/chapter/types-of-unit-cells-body-centered-cubic-and-face-centered-cubic-m11q5/ [Last accessed on October 23, 2025].

79. Radak M. Photolithography. Department of Physics, Iran University of Science and Technology; March 27, 2022. Available from: https://www.researchgate.net/publication/360258383 [Last accessed on October 23, 2025].

80. Mohamed LZ, El Kady OA, Lotfy MM, Ahmed HA, Elrefaie FA. Characteristics of Ni-Cr binary alloys produced by conventional powder metallurgy. *Key Eng Mater.* 2020;835:214-222.

doi: 10.4028/www.scientific.net/KEM.835.214

81. Jahangiri MR, Boutorabi SMA, Arabi H. Study on incipient melting in cast Ni base IN939 superalloy during solution annealing and its effect on hot workability. *Mater Sci Technol.* 2012;28(12):1402-1413.

    doi: 10.1179/1743284712Y.0000000090

82. Güler F, Şahin Kahraman A, Horasan B, Bilgin GM, Keleş Ö, Aydin H. Investigation of the Post-Processing Heat Treatments on Hot Tensile Properties of Selectively Laser Melted IN939 Superalloy. *Kocaeli J Sci Eng.* 2024;7(2):151-157.

    doi: 10.34088/kojose.1391406

83. Kumar EN, Athira KS, Chatterjee S, Srinivasan D. Effect of heat treatment on structure and properties of laser powder bed fusion Inconel 939. In: Proceedings of 2022 International Additive Manufacturing Conference, IAM 2022. American Society of Mechanical Engineers; 2022:1-9.

    doi: 10.1115/iam2022-93945

84. Ozer S, Doğu MN, Ozdemirel C, *et al.* Effect of aging treatment on the microstructure, cracking type and crystallographic texture of IN939 fabricated by powder bed fusion-laser beam. *J Mater Res Technol.* 2024;33:574-588.

    doi: 10.1016/j.jmrt.2024.09.106

85. Babinský T, Šulák I, Gálíková M, Kuběna I, Poloprudský J, Náhlík L. Room-temperature low-cycle fatigue behaviour of cast and additively manufactured IN939 superalloy. *Mater Sci Eng A*. 2025;924:147730.

    doi: 10.1016/j.msea.2024.147730

86. Šulák I, Gálíková M, Babinský T, Poczklán L, Kuběna I, Guth S. Thermomechanical fatigue performance of additively manufactured Inconel 939. *Int J Fatigue.* 2026;208:109552.

    doi: 10.1016/j.ijfatigue.2026.109552

87. Jiang Y, Li X, Du Y, *et al.* Defect tolerance in ultra-high cycle fatigue of additively manufactured IN939 alloy. *Eng Fract Mech*. 2025;316:110891.

    doi: 10.1016/j.engfracmech.2025.110891

88. Shahini MH, Kaveh A, Zhang B, *et al.* Measuring fatigue crack growth using microscale specimens: Si-modified Inconel 939 alloy processed by laser powder bed fusion additive manufacturing. *Mater Sci Eng A*. 2024;913:147032.

    doi: 10.1016/j.msea.2024.147032

89. Banoth S, Li CW, Hiratsuka Y, Kakehi K. The Effect of Recrystallization on Creep Properties of Alloy IN939 Fabricated by Selective Laser Melting Process. *Metals*. 2020;10(8):1016.

    doi: 10.3390/met10081016

90. DebRoy T, Mukherjee T, Milewski JO, *et al.* Scientific, technological and economic issues in metal printing and their solutions. *Nat Mater*. 2019;18(10):1026-1032.

    doi: 10.1038/s41563-019-0408-2

91. Manvatkar V, De A, Debroy T. Heat transfer and material flow during laser assisted multi-layer additive manufacturing. *J Appl Phys*. 2014;116(12):124905.

    doi: 10.1063/1.4896751

92. Manvatkar V, De A, DebRoy T. Spatial variation of melt pool geometry, peak temperature and solidification parameters during laser assisted additive manufacturing process. *Mater Sci Technol.* 2015;31(8):924-930.

    doi: 10.1179/1743284714Y.0000000701

93. Mukherjee T, Wei HL, De A, Debroy T. Heat and fluid flow in additive manufacturing—part II: powder bed fusion of stainless steel, and titanium, nickel and aluminum base alloys. *Comput Mater Sci.* 2018;150:369-380.

    doi: 10.1016/j.commatsci.2018.04.027

94. DebRoy T, David SA. Physical processes in fusion welding. *Rev Mod Phys*. 1995;67(1):85-112.

    doi: 10.1103/RevModPhys.67.85

95. Mukherjee T, DebRoy T. A digital twin for rapid qualification of 3D printed metallic components. *Appl Mater Today*. 2019;14:59-65.

    doi: 10.1016/j.apmt.2018.11.003.

96. Khairallah SA, Anderson AT. Mesoscopic simulation model of selective laser melting of stainless steel powder. *J Mater Processing Technol.* 2014;214(11):2627-2636.

    doi: 10.1016/j.jmatprotec.2014.06.001.

97. Lee YS, Zhang W. Modeling of heat transfer, fluid flow and solidification microstructure of nickel-base superalloy fabricated by laser powder bed fusion. *Addit Manuf.* 2016;12:178-188.

    doi: 10.1016/j.addma.2016.05.003

98. Knapp GL, Mukherjee T, Zuback JS, *et al.* Building blocks for a digital twin of additive manufacturing. *Acta Mater.* 2017;135:390-399.

    doi: 10.1016/j.actamat.2017.06.039

99. DebRoy T, Zhang W, Turner JA, Babu SS. Building digital twins of 3D printing machines. *Scr Mater.* 2017;135:119-124.

    doi: 10.1016/j.scriptamat.2016.12.005

100. Li Y, Gu D. Parametric analysis of thermal behavior during selective laser melting additive manufacturing of aluminum alloy powder. *Mater Des*. 2014;63:856-867.

    doi: 10.1016/j.matdes.2014.07.006

101. Foroozmehr A, Badrossamay M, Foroozmehr E, Golabi S. Finite Element Simulation of Selective Laser Melting process considering Optical Penetration Depth of laser in powder

bed. *Mater Des*. 2016;89:255-263.

doi: 10.1016/j.matdes.2015.10.002

102. Mukherjee T, Wei HL, De A, DebRoy T. Heat and fluid flow in additive manufacturing—Part I: Modeling of powder bed fusion. *Comput Mater Sci*. 2018;150:304-313.

doi: 10.1016/j.commatsci.2018.04.022.

103. Nie P, Ojo OA, Li Z. Numerical modeling of microstructure evolution during laser additive manufacturing of a nickel-based superalloy. *Acta Mater*. 2014;77:85-95.

doi: 10.1016/j.actamat.2014.05.039

104. Wei HL, Mukherjee T, Zhang W, *et al.* Mechanistic models for additive manufacturing of metallic components. *Prog Mater Sci*. 2021;116:100703.

doi: 10.1016/j.pmatsci.2020.100703

105. Yuan P, Gu D. Molten pool behaviour and its physical mechanism during selective laser melting of TiC/AlSi10Mg nanocomposites: Simulation and experiments. J *Phys D Appl Phys*. 2015;48(3):035303.

doi: 10.1088/0022-3727/48/3/035303

106. Keene BJ. Review of data for the surface tension of pure metals. *Int Mater Rev.* 1993;38(4):157-192.

doi: 10.1179/imr.1993.38.4.157

107. Pitscheneder W, DebRoy T, Mundra K, Ebner R. Role of sulfur and processing variables on the temporal evolution of weld pool geometry during multikilowatt laser-beam welding of steels. *Weld J*. 1996;75(3):71-80.

108. Tan W, Wen S, Bailey N, Shin YC. Multiscale modeling of transport phenomena and dendritic growth in laser cladding processes. *Metallurgical and Materials Transactions B: Process Metallurgy and Materials Processing Sci*. 2011;42(6):1306-1318.

doi: 10.1007/s11663-011-9545-y

109. Acharya R, Sharon JA, Staroselsky A. Prediction of microstructure in laser powder bed fusion process. *Acta Mater*. 2017;124:360-371.

doi: 10.1016/j.actamat.2016.11.018

110. Hu X, Nycz A, Lee Y, *et al.* Towards an integrated experimental and computational framework for large-scale metal additive manufacturing. *Mater Sci Eng A*. 2019;761:138057.

doi: 10.1016/j.msea.2019.138057

111. Zhang Z, Tan ZJ, Yao XX, *et al.* Numerical methods for microstructural evolutions in laser additive manufacturing. *Comput Math Appl.* 2019;78(7):2296-2307.

doi: 10.1016/j.camwa.2018.07.011

112. Ren N, Li J, Zhang R, *et al.* Solute trapping and non-equilibrium microstructure during rapid solidification of additive manufacturing. *Nat Commun*. 2023;14(1):7990.

doi: 10.1038/s41467-023-43563-x

113. Zeng C, Ding H, Bhandari U, Guo SM. Design of crack-free laser additive manufactured Inconel 939 alloy driven by computational thermodynamics method. *MRS Commun*. 2022;12(5):844-849.

doi: 10.1557/s43579-022-00253-x

114. Keller T, Lindwall G, Ghosh S, *et al.* Application of finite element, phase-field, and CALPHAD-based methods to additive manufacturing of Ni-based superalloys. *Acta Mater*. 2017;139:244-253.

doi: 10.1016/j.actamat.2017.05.003

115. Lindström T, Ewest D, Simonsson K, Eriksson R, Lundgren JE, Leidermark D. Constitutive model of an additively manufactured ductile nickel-based superalloy undergoing cyclic plasticity. *Int J Plast*. 2020;132:102752.

doi: 10.1016/j.ijplas.2020.102752

116. Ghoussoub JN, Tang YT, Dick-Cleland WJB, *et al.* On the Influence of Alloy Composition on the Additive Manufacturability of Ni-Based Superalloys. *Metall Mater Trans A Phys Metall Mater Sci*. 2022;53(3):962-983.

doi: 10.1007/s11661-021-06568-z

117. Martin JH, Yahata BD, Hundley JM, Mayer JA, Schaedler TA, Pollock TM. 3D printing of high-strength aluminium alloys. *Nature*. 2017;549(7672):365-369.

doi: 10.1038/nature23894

118. Li XP, Ji G, Chen Z, *et al.* Selective laser melting of nano-TiB2-decorated AlSi10Mg alloy with high fracture strength and ductility. *Acta Mater*. 2017;129:183-193.

doi: 10.1016/j.actamat.2017.02.062

119. Mukherjee T, Zuback JS, De A, DebRoy T. Printability of alloys for additive manufacturing. *Sci Rep*. 2016;6:19717.

doi: 10.1038/srep19717

120. Bidare P, Bitharas I, Ward RM, Attallah MM, Moore AJ. Fluid and particle dynamics in laser powder bed fusion. *Acta Mater*. 2018;142:107-120.

doi: 10.1016/j.actamat.2017.09.051

121. Ly S, Rubenchik AM, Khairallah SA, Guss G, Matthews MJ. Metal vapor micro-jet controls material redistribution in laser powder bed fusion additive manufacturing. *Sci Rep*. 2017;7:4085.

doi: 10.1038/s41598-017-04237-z

122. Leung CLA, Marussi S, Atwood RC, Towrie M, Withers PJ, Lee PD. In situ X-ray imaging of defect and molten pool dynamics in laser additive manufacturing. *Nat Commun*. 2018;9:1355.

doi: 10.1038/s41467-018-03734-7

123. Gunenthiram V, Peyre P, Schneider M, *et al.* Experimental analysis of spatter generation and melt-pool behavior during

the powder bed laser beam melting process. *J Mater Process Technol*. 2018;251:376-386.

doi: 10.1016/j.jmatprotec.2017.08.012

124. Basu S, DebRoy T. Liquid metal expulsion during laser irradiation. *J Appl Phys*. 1992;72(8):3317-3322.

doi: 10.1063/1.351452

125. Matthews MJ, Guss G, Khairallah SA, Rubenchik AM, Depond PJ, King WE. Denudation of metal powder layers in laser powder bed fusion processes. *Acta Mater*. 2016;114:33-42.

doi: 10.1016/j.actamat.2016.05.017

126. Guo Q, Zhao C, Escano LI, *et al.* Transient dynamics of powder spattering in laser powder bed fusion additive manufacturing process revealed by in situ high-speed high-energy x-ray imaging. *Acta Mater.* 2018;151:169-180.

doi: 10.1016/j.actamat.2018.03.036

127. Wang L, Feng S, Wang Y, *et al.* Porosity defects in additively manufactured metal materials: Formation mechanisms, impact on performance and regulation. *Proc Inst Mech Eng Part C J Mech Eng Sci.* 2025;71(2).

doi: 10.1177/09506608251371459

128. Youngs DL. Time-Dependent Multi-Material Flow with Large Fluid Distortion. In: Morton KW, Baines MJ, eds. *Numerical Methods for Fluid Dynamics*. Academic Press; 1982:273-285.

129. Zhou X, Wang D, Liu X, *et al.* 3D-imaging of selective laser melting defects in a Co-Cr-Mo alloy by synchrotron radiation micro-CT. *Acta Mater*. 2015;98:1-16.

doi: 10.1016/j.actamat.2015.07.014

130. Kasperovich G, Haubrich J, Gussone J, Requena G. Correlation between porosity and processing parameters in TiAl6V4 produced by selective laser melting. *Mater Des*. 2016;105:160-170.

doi: 10.1016/j.matdes.2016.05.070

131. Cunningham R, Narra SP, Ozturk T, Beuth J, Rollett AD. Evaluating the Effect of Processing Parameters on Porosity in Electron Beam Melted Ti-6Al-4V via Synchrotron X-ray Microtomography. *JOM*. 2016;68(3):765-771.

doi: 10.1007/s11837-015-1802-0

132. Aboulkhair NT, Everitt NM, Ashcroft I, Tuck C. Reducing porosity in AlSi10Mg parts processed by selective laser melting. *Addit Manuf*. 2014;1:77-86.

doi: 10.1016/j.addma.2014.08.001

133. Attallah MM, Jennings R, Wang X, Carter LN. Additive manufacturing of Ni-based superalloys: The outstanding issues. *MRS Bull*. 2016;41(10):758-764.

doi: 10.1557/mrs.2016.211

134. Tammas-Williams S, Zhao H, Léonard F, Derguti F, Todd I, Prangnell PB. XCT analysis of the influence of melt strategies on defect population in Ti-6Al-4V components manufactured by Selective Electron Beam Melting. *Mater Charact*. 2015;102:47-61.

doi: 10.1016/j.matchar.2015.02.008

135. Carter LN, Martin C, Withers PJ, Attallah MM. The influence of the laser scan strategy on grain structure and cracking behaviour in SLM powder-bed fabricated nickel superalloy. *J Alloys Compd*. 2014;615:338-347.

doi: 10.1016/j.jallcom.2014.06.172

136. Uddin SZ, Murr LE, Terrazas CA, Morton P, Roberson DA, Wicker RB. Processing and characterization of crack-free aluminum 6061 using high-temperature heating in laser powder bed fusion additive manufacturing. *Addit Manuf*. 2018;22:405-415.

doi: 10.1016/j.addma.2018.05.047

137. Gu D, Hagedorn YC, Meiners W, *et al.* Densification behavior, microstructure evolution, and wear performance of selective laser melting processed commercially pure titanium. *Acta Mater*. 2012;60(9):3849-3860.

doi: 10.1016/j.actamat.2012.04.006

138. Sun G, Zhou R, Lu J, Mazumder J. Evaluation of defect density, microstructure, residual stress, elastic modulus, hardness and strength of laser-deposited AISI 4340 steel. *Acta Mater*. 2015;84:172-189.

doi: 10.1016/j.actamat.2014.09.028

139. Harrison NJ, Todd I, Mumtaz K. Reduction of micro-cracking in nickel superalloys processed by Selective Laser Melting: A fundamental alloy design approach. *Acta Mater*. 2015;94:59-68.

doi: 10.1016/j.actamat.2015.04.035

140. Chauvet E, Kontis P, Jägle EA, *et al.* Hot Cracking Mechanism Affecting a Non-Weldable Ni-Based Superalloy Produced by Selective Electron Beam Melting. *Acta Mater*. 2018;142:82-94.

doi: 10.1016/j.actamat.2017.09.047

141. Qiu C, Adkins NJE, Attallah MM. Selective laser melting of Invar 36: Microstructure and properties. *Acta Mater*. 2016;103:382-395.

doi: 10.1016/j.actamat.2015.10.020

142. Kou S. A criterion for cracking during solidification. *Acta Mater.* 2015;88:366-374.

doi: 10.1016/j.actamat.2015.01.034.

143. Young GA, Capobianco TE, Penik MA, Morris BW, McGee JJ. The mechanism of ductility dip cracking in nickel-chromium alloys. *Weld J*. 2003;82(6):101S-110S.

144. Chen Y, Zhang K, Huang J, Hosseini SRE, Li Z. Characterization of heat affected zone liquation cracking

in laser additive manufacturing of Inconel 718. *Mater Des*. 2016;90:586-594.

doi: 10.1016/j.matdes.2015.10.155

145. Chen Y, Lu F, Zhang K, *et al.* Dendritic microstructure and hot cracking of laser additive manufactured Inconel 718 under improved base cooling. *J Alloys Compd*. 2016;670:312-321.

doi: 10.1016/j.jallcom.2016.01.250

146. Ramirez AJ, Lippold JC. High temperature behavior of Ni-base weld metal Part I. Ductility and microstructural characterization. *Mater Sci Eng A*. 2004;380(1-2):259-271.

doi: 10.1016/j.msea.2004.03.074

147. Noecker FF II. Metallurgical Investigation into Ductility Dip Cracking in Ni-Based Alloys. PhD dissertation. Bethlehem, PA: Lehigh University; 2007.

148. Xia M, Gu D, Yu G, Dai D, Chen H, Shi Q. Porosity evolution and its thermodynamic mechanism of randomly packed powder-bed during selective laser melting of Inconel 718 alloy. *Int J Mach Tools Manuf*. 2017;116:96-106.

doi: 10.1016/j.ijmachtools.2017.01.005

149. Qiu C, Panwisawas C, Ward M, Basoalto HC, Brooks JW, Attallah MM. On the role of melt flow into the surface structure and porosity development during selective laser melting. *Acta Mater*. 2015;96:72-79.

doi: 10.1016/j.actamat.2015.06.004

150. Yan W, Ge W, Qian Y, *et al.* Multi-physics modeling of single/multiple-track defect mechanisms in electron beam selective melting. *Acta Mater*. 2017;134:324-333.

doi: 10.1016/j.actamat.2017.05.061.

151. Khairallah SA, Anderson AT, Rubenchik A, King WE. Laser powder-bed fusion additive manufacturing: physics of complex melt flow and formation mechanisms of pores, spatter, and denudation zones. *Acta Mater*. 2016;108:36-45.

doi: 10.1016/j.actamat.2016.02.014.